Chapter 8
The Plumes and Atmosphere of Io

Imke de Pater, David Goldstein, and Emmanuel Lellouch

Abstract The current state of knowledge of Io's atmosphere and plumes is summarized, with an emphasis on research conducted since the *Galileo* era. While the primary source of Io's atmosphere is sublimation of SO_2 frost, at times and/or locally volcanoes have a substantial effect on the atmosphere (and sometimes dominate), as shown both via observations and model simulations. The effect of sputtering is less clear, but may be important at high latitudes, and perhaps at night and during eclipse. Photodissociation is likely the primary source of SO, Na, K, and Cl but S_2's main source is volcanic, primarily from "Pele-type" volcanism. While the primary source of NaCl and KCl is most likely volcanic, it is not clear how much sputtering may contribute to the emissions. Some of the NaCl and KCl appears to originate from volcanic vents that do not expel much, if any, SO_2 gas.

A comparison between data and models shows that atmospheric collapse upon eclipse ingress and its reformation upon egress happens much faster than models indicate. The observed brightening and expansion of the SO_2 emissions near volcanic plumes upon eclipse egress, however, does agree with models. Data nor models (at the same resolution) show an enhancement in column density above a plume. As shown in this review, although considerable progress has been made towards both a characterization and understanding of Io's atmosphere, there are some fundamental questions that need to get answered before we can truly understand and simulate all physical processes that contribute to both the composition of and dynamics in Io's atmosphere.

I. de Pater (✉)
Department of Astronomy, & Department of Earth and Planetary Science, University of California, Berkeley, CA, USA
e-mail: imke@berkeley.edu

D. Goldstein
Department of Aerospace Engineering, University of Texas at Austin, Austin, TX, USA
e-mail: david@oden.utexas.edu

E. Lellouch
Laboratoire d'Études Spatiales et d'Instrumentation en Astrophysique (LESIA), Observatoire de Paris, Meudon, France
e-mail: Emmanuel.Lellouch@obspm.fr

R. M. C. Lopes et al. (eds.), *Io: A New View of Jupiter's Moon*, Astrophysics and Space Science Library 468, https://doi.org/10.1007/978-3-031-25670-7_8

Keywords Io · Volcanoes · Atmosphere composition · Atmospheric dynamics

8.1 Introduction

The first evidence for the existence of an atmosphere on Io was obtained in 1973, when the *Pioneer 10* spacecraft detected ionospheric layers above Io's surface near its terminator (Kliore et al. 1974). This was soon followed by a detection of sodium (Brown 1974) and potassium (Trafton 1975) in a cloud around Io. This "neutral" cloud extends along a part of Io's orbit, and due to the Keplerian motion of the particles this cloud is shaped like a banana. Upon ionization, the species are swept away by Jupiter's magnetic field, forming the Io plasma torus. The sodium, potassium as well as the sulfur ions detected in the plasma torus (Kupo et al. 1976) were, at the time, hypothesized to originate on Io.

About a decade before the *Pioneer 10* flyby, Binder and Cruikshank (1964) reported that Io was much brighter in reflected sunlight immediately after eclipse egress than 10–20 min later. The authors hypothesized the presence of an atmosphere, condensing into bright frost on the surface while in eclipse, and subliming upon egress, causing the surface to darken again. However, even though we now know that Io has a mostly condensible atmosphere, the reality of the eclipse brightening events remains controversial, as subsequent data have not shown this effect (e.g., Secosky and Potter 1994).

In 1979, when *Voyager 1* flew by, it imaged volcanic plumes above Pele and Loki, the latter a lava flow to the north-east of the horseshoe-shaped caldera Loki Patera (Morabito et al. 1979). Interestingly, just prior to taking these images, Peale et al. (1979) had predicted large amounts of tidal heat dissipation in Io's interior caused by the fact that Io, Europa and Ganymede are locked in a 4:2:1 orbital (Laplace) resonance which creates a significant forced eccentricity in their orbits. Peale et al. (1979) had predicted the *Voyager* spacecraft would detect effects from the resulting high heat flow on Io's surface, a prediction that was confirmed in record time.

In addition to the visible plumes, Pearl et al. (1979) reported the presence of SO_2 gas above Loki based upon an analysis of *Voyager 1*/IRIS spectra, which showed a 7.3 μm absorption feature against a warm thermal background. Since this was the only time such spectra were obtained against a warm background, it was not clear if SO_2 was confined to this volcanically active spot or was more widespread across the satellite. It took another decade before Io's "global" SO_2 atmosphere was observed. This was accomplished from the ground, using the IRAM-30 m telescope at 1.4 and 2.0 mm (222 and 143 GHz) (Lellouch et al. 1990, 1992). In their initial analysis, these data revealed a surface pressure of order 3–40 nbar (column densities of 1.5×10^{17}–2×10^{18} cm^{-2}), covering only a fraction of Io's surface (3–20%) at a high gas temperature (∼500–600 K).

Since that time Io's atmosphere and plumes have been observed across the electromagnetic spectrum, from the UV through mm-wavelengths, from the ground, near-Earth orbit, and the *Galileo*, *Cassini*, and *New Horizons* spacecraft. Excellent

early—before *Galileo*—reviews have been published by, e.g., Spencer and Schneider (1996) and Lellouch (1996), while papers by McGrath et al. (2004), Geissler and Goldstein (2007) and Lellouch et al. (2007) present reviews on Io's plumes and atmosphere after completion of the *Galileo* mission. The present review is focused on results obtained since the *Galileo* era, although some early results will be mentioned to present a coherent picture.

We start below with an overview of Io's global atmospheric properties, including a short summary of observational methods, and timescales relevant to atmospheric physics and chemistry. In Sect. 8.3 we present an overview of the spatial distribution of Io's atmospheric gases, including views when Io is in eclipse. Observations and models of plumes are discussed in Sect. 8.4. Finally, in Sect. 8.5, we address the question: "What drives Io's atmosphere", and discuss the arguments in favor of a sublimation-driven and volcanically-driven atmosphere, as well as the conditions under which one might expect sputtering to be important. The chapter ends with conclusions (Sect. 8.6), a list of open questions, and future directions.

8.2 Global Atmospheric Properties

Io's atmosphere has been observed at multiple wavelengths and with a variety of techniques, each with their own advantages and shortcomings. An overview of available data is given in Table 8.1. In order to better assess the interpretation of these data we provide a short summary of the pros and cons for each technique in Sect. 8.2.1. This section is followed by a short review of timescales as relevant both to observations and models of the atmosphere and plumes. We end this section with summaries of the global composition and thermal structure of the atmosphere.

8.2.1 Observational Methods

(1) Millimeter/Submillimeter At mm/submm-wavelengths one detects thermal emission from the atmosphere, typically 20–40 K above the background (sub-)surface brightness temperature (∼95 K; Moullet et al. 2008; de Pater et al. 2020b) for disk-integrated data. The emissions occur in local thermodynamic equilibrium (LTE) (Lellouch et al. 1992), i.e. energy levels are populated according to atmospheric physical temperatures. Hence, by observing different transitions and measuring line widths and line contrasts, one should, in principle, be able to determine gas temperature, column density, and fractional coverage of the atmosphere, where the latter refers either to the disk as a whole or to the spatial element provided by the data. However in practice most observed transitions have similar (low) energy levels, which to date has precluded accurate temperature measurements. Moreover, the interpretation of line shapes, indicative of temperature through thermal broadening, is complicated by velocity broadening and/or line

Table 8.1 Molecular observations of Io's atmosphere and plumes

Wavelength	Telescope/Instrument	Sp/Im[a]	Resolution[b]	Constituents	Sensitivity[c]	Sunlight/eclipse	References
Mm (1–3 mm)	IRAM-30m	Sp	Disk	SO_2, SO, NaCl	N, T, v, f	sunlight	17–20
Mm (1 mm)	IRAM PdBI	Sp	Cube	SO_2	N, T, v, f	sunlight	23
Mm (1 mm)	IRAM NOEMA	Sp	Disk	SO_2, NaCl	N, T, v, f	sunlight	29
Submm (0.8 mm)	APEX	Sp	Disk	SO_2, SO, KCl	N, T, v, f	sunlight	25
Submm (0.8 mm)	SMA	Sp	Cube	SO_2, SO, NaCl	N, T, v, f	sunlight	24
Submm (0.8 mm)	ALMA	Sp	Cube	SO_2, SO, NaCl, KCl	N, T, v, f	sunlight/eclipse	7
Mid-IR 19 μm	IRTF/TEXES	Sp	Disk	SO_2 (ν_2 band)	N, T	sunlight/eclipse	34,38,39,40,42
Mid-IR 7.3 μm	Voyager/IRIS	Sp	Res	SO_2 (ν_3 band)	N, T	sunlight	26
Near-IR 4 μm	VLT/CRIRES	Sp	Cube	SO_2 ($\nu_1 + \nu_3$ band)	N, *T*	sunlight	21
Near-IR 1.7 μm	Keck/NIRSPEC	Sp	Disk, Res	SO	N, *T*	eclipse	3–5, 16
Near-IR 1.7 μm	Keck/OSIRIS	Sp	Cube	SO	N, *T*	eclipse	6
Visible	Voyager, Galileo, Cassini, New Horizons	Im	Res	Plumes	Opacity, part. size	Sunlight	10
UV 0.255, 0.336, 0.410 μm	HST/WFC2	Im	Res	Plume, S_2, SO_2	Opacity, part. size	sunlight	14,32,33,
UV 0.232, 0.260 μm	HST/FOC	Im	Res	SO_2	N	sunlight	30,31
UV 0.225–0.330 μm	HST/FOS	Sp	Disk	SO2	N, f	sunlight	2
UV 0.210–0.320 μm	Galileo/UVS	Sp	Res	SO_2	N	sunlight	12
UV, 0.210–0.310 μm	HST/STIS	Sp	Res	SO_2	N, *T*	sunlight	13,15
UV 0.210–0.234 μm	HST/COS	Sp	Disk	SO_2	N, *T*, f	post-eclipse	41
UV 0.202-0.233	HST/COS.	Sp.	Disk.	SO_2.	N, *T*, f.	sunlight.	40
UV 0.197–0.235 μm	HST/FOS and GHRS	Sp	Disk	SO_2	N, *T*, f	sunlight	1,37
UV 0.180–0.310 μm	HST/STIS	Sp	Res	S_2, SO_2	N, *T*	transmission	33

UV-Vis 0.175–0.570 μm	HST/STIS	Sp	Res	S, SO, SO_2	N, torus prop.	eclipse	36
UV 0.159–0.231 μm	HST/FOS	Sp	Res	SO_2, S, SO	N, *T*	sunlight	22
UV 0.121 μm (Lyα)	HST/STIS	Im	Res	SO_2	N	sunlight	8,9,11,35,28
UV 0.121 μm (Lyα)	HST/STIS	Im	Res	SO_2	N	transmission	27

References: 1: Ballester et al. 1994; 2: Clarke et al. 1994; 3: de Kleer et al., 2019c; 4: de Pater et al. 2002; 5: de Pater et al. 2007; 6: de Pater et al. 2020a; 7: de Pater et al. 2020b; 8: Feaga et al. 2009; 9: Feldman et al. 2000; 10: Geissler and Goldstein 2007; 11: Giono and Roth 2021; 12: Hendrix et al. 1999; 13: Jessup et al. 2007; 14: Jessup and Spencer 2012; 15: Jessup and Spencer 2015; 16: Laver et al. 2007; 17: Lellouch et al. 1990; 18: Lellouch et al. 1992; 19: Lellouch et al. 1996; 20: Lellouch et al. 2003; 21: Lellouch et al. 2015; 22: McGrath et al. 2000; 23: Moullet et al. 2008; 24: Moullet et al. 2010; 25: Moullet et al. 2013; 26: Pearl et al. 1979; 27: Retherford et al. 2019; 28: Roessler et al. 1999; 29: Roth et al. 2020; 30: Sartoretti et al. 1994; 31: Sartoretti et al. 1996; 32: Spencer et al. 1997; 33: Spencer et al. 2000; 34: Spencer et al. 2005; 35: Strobel and Wolven 2001; 36: Trafton et al. 2012; 37: Trafton et al. 1996; 38: Tsang et al. 2012; 39: Tsang et al. 2013a; 40: Tsang et al. 2013b; 41: Tsang et al. 2015; 42: Tsang et al. 2016

[a] Spectra (Sp) or Images (Im)

[b] Disk-integrated (Disk), spatially resolved (Res), or spectral data cube (Cube)

[c] Sensitivity of observations to the column density (N), velocity (v), fractional coverage (f), and temperature (T), where T refers to direct sensitivity to temperature through the Planck function, while *T* refers to indirect sensitivity through line parameters or cross-sections

shifts due to local or global winds (Sect. 8.4.1). The main drawback of mm/submm observations, namely the lack of spatial resolution for single-dish antennas, is currently being overcome by the use of interferometers (e.g., de Pater et al. 2020b).

(2) Ultraviolet/Visible At UV-visible wavelengths Io is seen in reflected sunlight. Since the solar UV flux drops steeply with decreasing wavelength below ~400 nm, reflected emission from Io's disk decreases sharply as well, with the exception of the Ly-α line (121.6 nm), which shows a spike in solar emission. Both SO_2 gas and surface frost absorb strongly at UV wavelengths. As discussed in Sect. 8.3, the morphology of Io images in the Ly-α line has been used to derive the SO_2 abundance and its spatial extent.

UV data of Io include imaging, disk-averaged and disk-resolved spectroscopy. At low spectral resolution (and even more in imaging), it is difficult to disentangle the surface and atmosphere contributions, mostly because the surface reflectance depends strongly on unknown properties such as grain size and state of mixing of SO_2 frost. Off-limb observations of Io transiting Jupiter are immune to contamination from Io's surface, but require high spatial resolution in the UV/optical (Spencer et al. 2000). Even then, interpretation of plume brightness may be complicated by competing absorption between dust and gas.

At the low brightness of Io's disk at UV wavelengths away from solar lines, Io's aurora are prominent. When the satellite is observed in eclipse, its reflected component disappears completely, and even faint auroral emissions become visible (see Sect. 8.3.3 for details).

Unlike in the thermal range, atmospheric features in the UV are primarily sensitive to the column density of the atmospheric gas and the intensity of the electrical currents that excite auroral emissions (Sect. 8.3.3), but not directly to the gas temperature, although band contrasts, positions and skewness, do show a temperature dependence (Wu et al. 2000).

(3) Mid-infrared SO_2 ro-vibrational lines have been detected in the (thermal) mid-infrared (ν_2 band at 19 μm, ν_3 band at 7.3 μm). Unlike rotational levels, vibrational levels can be populated by direct solar excitation and absorption of surface thermal flux, and are strongly subject to non-LTE effects, with radiative de-excitation timescales shorter than collisional timescales (Lellouch et al. 1992; Spencer et al. 2005). So far, these bands have only been seen in absorption, indicating vibrational temperatures colder than the surface temperature, even though most of the atmosphere is expected to be at physical temperatures higher than the surface (see below Sect. 8.2.4). On the other hand, rotational LTE is expected in the lower atmosphere (see Fig. 8.1), enabling one to determine the translational/rotational temperature of the atmosphere from the relative strengths between the lines in a band, although optical depth effects may occur (see, e.g., Fig. 6 in Tsang et al. (2012)).

(4) Near-infrared SO_2 gas has also been detected in its $\nu_1 + \nu_3$ band at 4.0 μm, with spatial information (Lellouch et al. 2015). Being located in the dominantly solar-reflected part of Io's spectrum, it appears in absorption and interpretation is relatively straightforward in terms of SO_2 columns and temperature, because

lines are optically thin (∼0.1 opacity at infinite resolution) and numerous energy transitions are observed. Absorptions are rather faint, however, and intermixed with telluric and solar lines, requiring an instrument with both high sensitivity and high resolving power (e.g. VLT/CRIRES).

Observations of Io in eclipse have revealed emissions from SO in the near-infrared, discussed in Sect. 8.3.2.

8.2.2 Timescales Relevant to Observations and Modeling

In this section we review the physical time scales relevant to observations and modeling of Io's atmosphere and plumes. Table 8.2 is a breakdown of several such time scales, from shortest at molecular scales up to an Ionian year (#A–O), with comments on associated length scales and physics.

Molecular/Atomic Time Scales Plasma ions traveling at tens of km/s cross spatial density gradients of neutral species in times of O(1E-3 to 1E-2 s) (McDoniel et al. 2019): if it is important to resolve plasma interactions with a density gradient in a simulation then the time step must be less than that (A). Ion or fast neutrals from charge exchange suffer collisions in dense gas regions near the ground with time scales of less than O(1E-2 s) (the mean collision time); however, above the exobase this time scale rises to minutes (Walker et al. 2010) (B). The half-life of SO_2 vibration modes to spontaneous emission varies from milliseconds (i.e., virtually instantaneous on a gas-dynamic time scale) to ∼1 s, a time over which hot gas in a plume could move a kilometer or more (Zhang et al. 2003) (C). The cyclotron gyration time of ions in the local magnetic field is roughly half a second—during which time the ion may travel quite a distance, depending on the local gas density and mean free path (McDoniel et al. 2019) (D). The mean collision time for thermal neutrals in a nominal sublimation atmosphere varies from $O(0.1\,\mathrm{s})$ near the surface at equatorial noon to arbitrarily long (escape) above the exobase (E). The residence time of an SO_2 molecule stuck on the surface governs how readily gas condenses on or is released from the surface (Walker et al. 2012); that time scale varies from a few seconds or less (effectively producing a simple diffusely scattering surface) to hours or more on the night side or at high latitudes (those surfaces thus act as local cold traps) (F). Molecules rising from the surface would have a ballistic time (their rise/fall time) determined by gravity and their launch speed and angle. That speed is set by the temperature of the surface. For the cool sources of atmospheric molecules at ∼100–150 K, the ballistic time ($\approx 2\sqrt{2RT_{source}/m}/g$) is 3–4 min while in a large Pele-class plume sourced from hot magma, with $T_{source} \approx 1200$ K, the time is $\approx 2\sqrt{2CpT_{source}}/g$. Here, Cp is the specific heat, R the universal gas constant, m the molecular mass, and g the surface gravity, and the resulting ballistic time is about 20 min (G). The photodestruction (dissociation or ionization) time scales for different observable molecules is several hours or more (L).

Table 8.2 Time scales and physics relevant to both observations and models

	Physical process	Timescale	Modeling time step required	Length and velocity scales setting the time scale	Relation to atmospheric or plume dynamics and observations
A	Plasma interactions with atm. and plumes	< 0.1 s	< 0.1 s	Atm/plume density gradients like atm. scale height or plume dimensions and plasma particle speeds	Plasma interactions with atm/plume which are not simply plane-parallel and 1-dimensional
B	Ion/neutral collision rates	$\gtrsim$0.01 s	$\gtrsim$0.01 s	Lengths set by neutral density and collision cross sections (ion mean free path) and ion speeds	Determines local chemical rates and ion-impact induced emission
C	Molecular vibration or rotation half-life	millisec-to-sec	Stochastic, based on Einstein-A, but < lifetime of 10^{-3}–1 s	NA—a fundamental molecular property	Determines where thermal emission occurs and whether process is in LTE
D	Cyclotron gyration	~0.5 s for ions	0.1 s	Set by ion mass, charge and $\|\|B\|\|$	Related to Hall effects, emission from atm. and plumes
E	Neutral gas motion	0.1 s +	0.01 s +	Local density through mean free path and local field property gradients	Links between macroscopic gas dynamics (shock waves, scale heights, shear layers, and flows created by surface contrasts) and molecular collision MFP
F	Gas-Surface interaction	Residence time of molecules on solid surfaces	<0.1 s to years	NA—a fundamental material property	Varies with species, surface temperature, surface nature. Governs whether or when surface is a sink or diffuse
G	Molecular ballistic time	1 to >20 minutes	1 s–2 min	Set by surface gravity and vertical launch speed (hence, surface temperature)	Very different in plumes and sublimation atm. Sets effective height of both

H	Plume flow evolution	>20 min for Pele-class plumes	Few sec. since plume details are not determined just by ballistics	Over a cold surface acting as a material sink, set by ballistic time	Plumes initiate (rise and fall) on ballistic times; can be much longer if plume bounces off surface or atmosphere
I	Atmos. vertical flow evolution.	<10 min.	Few seconds, constrained by molecular collision times	Related to atm. ballistic time and hence scale height and speed of sound	Atm. collapse and recovery around eclipse occurs through vertically propagating waves
J	Atmos. horizontal flow evolution.	1 h	Few seconds, constrained by molecular collision times	Related to atm. horizontal pressure gradients, felt at speed of sound and are of planet-scale	Pressure-driven winds form due to weak pressure gradients over long distances
K	Eclipse time	2 h	NA	NA—fundamental property	Affects surface temperatures and photodissociation and thus winds and column
L	SO_2, SO, NaCl, KCl photodestruction (transparent atm)	SO_2: 34 h SO: 17 h NaCl: 3 h KCl: 2.5 h	Stochastic, based on rates at 5 to 5.5 AU	NA - fundamental property	Important for production of daughter species S, O, Na, K, Cl
M	One Io day	42 h	NA	NA—fundamental property	Sublimation components presumably periodic over a day/night
N	Atmos. loss to torus	~10 days	0.1 s for sputtering	NA	Set by atm loss rate and inferred by torus luminosity
O	One Io year	12 Earth years	NA	NA—fundamental property	Sublimation components have seasonal variation

Gas Dynamic Time Scales We next consider gas-dynamic or flow time scales: The flow evolution time in a plume (the time it would take for a plume to develop out to its main deposition ring if the plume were abruptly turned on) is about the same as the ballistic time, ∼20 min for Pele or Tvashtar (H). On the other hand, the formation time for portions of the plume which undergo a gasdynamic "bounce" (Zhang et al. 2003) or which spread out atop a lower level sublimation atmosphere (McDoniel et al. 2017) could be appreciably longer. The sublimation component of the atmosphere has at least two different flow evolution time scales, which are associated with two different length scales and the speed of sound, c_s, in SO_2 at the local surface temperature.[1] For vertical motions relevant to atmospheric collapse and reformation around eclipse, the appropriate length scale is the atmospheric scale height H,[2] which is ∼10 km near the surface, and the time scale is $\sim H/c_s$, i.e., the atmosphere is expected to collapse on a time scale of ∼70 s (Summers and Strobel 1996; de Pater et al. 2002), assuming the surface cools instantaneously (I). The second relevant gasdynamic timescale is the hydrostatic adjustment time c_s/g, which is ∼100 s. This few minute time scale is comparable to the thermal response time of the surface to eclipse ingress/egress.

The response of the surface temperature to changes in illumination depends upon the thermal inertia of the surface. Tsang et al. (2016) showed that the surface temperature dropped essentially instantaneously upon eclipse ingress, which has been used to show that the thermal inertia of the surface is quite low (see Sects. 8.3.2 and 8.5.1). The time for the formation of global pressure-driven winds should scale with the speed of sound and a *global* length scale such as Io's radius, R_{Io}, since it is over that length that illumination (and hence pressure) changes appreciably: $R_{Io}/c_s \sim 3.3$ h (J). This scale is comparable to the time scale of a Jovian eclipse itself, ∼2 h (K), suggesting that the winds will be changing during eclipse and for a couple of hours thereafter. A second time scale coincidence which may have unrecognized impact on the diurnal evolution of the global scale flow is that the optically thin photo-dissociation time of SO_2, generally into SO and O, is ∼34 h (L), comparable to Io's 42 h day/night cycle. The photodestruction time for SO is about half that—17 h, while for NaCl and KCl it is ∼3 and 2.5 h, resp. (Moses et al. 2002a,b). Near-surface atmospheric layers will be shielded and dissociate more slowly.

A more complete discussion of the time scales relevant to atmospheric composition is provided in Summers and Strobel (1996).

[1] $c_s = \sqrt{\gamma RT_{surf}/m}$, where γ is the ratio of specific heats.

[2] The scale height $H = RT(z)/g/m$, with $T(z)$ the temperature at altitude z. $H \sim 10$ km at temperature $T \simeq 140$ K.

8.2.3 Atmospheric Composition

The primary constituent of Io's atmosphere as observed to date is SO_2 gas, a common terrestrial volcanic species and a species notably able to exist in solid/vapor phases at common surface and near-surface pressure/temperature conditions on Io. Photodissociation of SO_2 produces primarily SO and atomic O (Summers and Strobel 1996; Moses et al. 2002a), both of which have been detected (SO by Lellouch et al. (1996); O by Brown (1981)) at abundance ratios with SO_2 between ~3–10% for SO (Lellouch et al. 2007), and ~10% for O (Roth et al. 2014). It is unclear, though, if all observed SO is produced through photochemistry, since it can also be produced directly in volcanic eruptions (Zolotov and Fegley 1998). SO does not have a condensed form, and its losses include recombination to SO_2 and photolysis to O and S, the latter being detected at ~2% of the SO_2 level (Roth et al. 2014). Although photodissociation of SO_2 also predicts some O_2, the column-integrated production rate of O_2 is about 2 orders of magnitude less than that of SO and O (Moses et al. 2002a). This, combined with its destruction primarily through reactions with atomic S, predicts O_2 to be at the ~1% level of SO_2.

S_2 was directly detected on one occasion via *HST* imaging and spectroscopy of Pele's plume on Io's limb against Jupiter, at an S_2/SO_2 ratio of 0.08–0.3 (Spencer et al. 2000). S_2 has a very short photochemical lifetime, and since it has no solid phase, its presence can only be attributed to volcanic activity (Zolotov and Fegley 1998; Moses et al. 2002a); moreover, it has only been detected above (a few) volcanic vents (Sect. 8.4.1). Based on thermochemical equilibrium models (Zolotov and Fegley 1999, 2000), the measured S_2/SO_2 ratio is consistent with equilibration in silicate magmas at 1400–1800 K.

Early this century, atomic chlorine (Retherford 2002; Feaga et al. 2004) was detected in Io's atmosphere at a typical abundance ratio with SO_2 of $\sim 5 \times 10^{-4}$, followed by the discovery of NaCl (Lellouch et al. 2003) and KCl (Moullet et al. 2013). The latter two constituents are likely the source of the atomic species (Na, K) that were detected in the 1970s in Io's neutral clouds (Sect. 8.1), as well as Cl. The typical relative abundances of NaCl and KCl to SO_2 (assuming co-location, which is now known to not be the case, Sect. 8.5.3) are $\sim 3 \times 10^{-3}$ and $\sim 5 \times 10^{-4}$, respectively. Since the photochemical lifetime for both species is relatively short ($\lesssim$3 h, Table 8.2; Moses et al. 2002b), both species need to be sourced (quasi-) continuously. However, whether NaCl and KCl are purely volcanic in origin, or may also result from sputtering on Io's surface has not yet been resolved (see Sect. 8.5.3 for more discussions).

Finally, a few additional compounds have been unsuccessfully searched for at mm-wavelengths (CO, H_2S, OCS, S_2O, ClO, CS, NaOH, SiO) or in the UV (CS_2). These searches have notably led to an upper limit of 10^{-10} bar for H_2S (Lellouch et al. 1992), another common volcanic species on Earth, ruling out the case for a H_2S global atmosphere on Io.

8.2.4 Thermal Structure

The thermal structure of Io's atmosphere mostly reflects the interplay between heating processes, radiative losses to space, and exchanges (radiative, conductive and convective) between atmospheric layers. As discussed in Sect. 8.5.1, an important fraction of Io's atmosphere is sublimation supported, and initial studies of Io's thermal structure (Lellouch et al. 1992; Strobel et al. 1994) have considered a 1D sublimation atmosphere in hydrostatic equilibrium, with adjustable surface temperature. The surface pressure over SO_2 ice is equal to the saturated vapor pressure of SO_2, which is a steep exponential function of temperature: $P_{vapor} = 1.52 \times 10^8 e^{-4510/T}$ bar (Wagman 1979).

Absorption of sunlight by SO_2 gas occurs at UV and infrared wavelengths, and radiative cooling from ro-vibrational bands and rotational lines at infrared and radio wavelengths. Non-LTE effects, which come into play at altitudes where the radiative de-excitation timescale is shorter than the collisional excitation timescale (Table 8.2), significantly affect the cooling terms, especially vibrational, while rotational LTE is maintained at least in the first few scale heights (see Fig. 8.1). Despite the reduced cooling efficiency associated with non-LTE, Strobel et al. (1994) argued that at large local pressures (>10 nbar), vibrational cooling in the ν_2 19-μm band is sufficient for a ~10 K decrease with altitude in the bottom 10–20 km of the atmosphere. At higher levels, rotational cooling takes over, but also progressively becomes non-LTE, and in the presence of solar heating only, the temperature asymptotically reaches ~275 K. Strobel et al. (1994) demonstrated the importance of Joule and plasma heating at the top of Io's atmosphere, and showed that temperatures could rise up to ~1800 K at several hundreds of kilometers

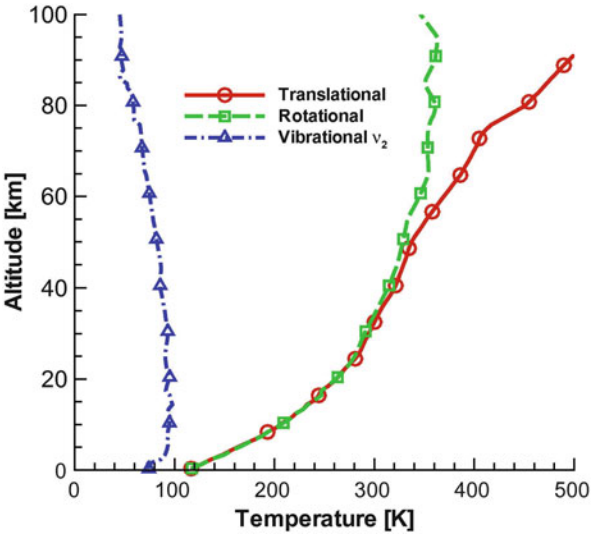

Fig. 8.1 Simulated thermal structure in the lower 100-km of Io's atmosphere above the sub-solar point based on the 3-D simulations by Walker et al. (2010). A 115 K subsolar surface (ice) temperature was adopted (i.e., the surface pressure was ~1.4 nbar), as well as a plasma heating source from above. The vibrational, rotational and translational (i.e. kinetic) temperatures are shown (from Gratiy et al. 2010)

above the surface. These 1-D models were later updated within self-consistent 3-D sublimation models of Io's atmosphere, leading to the prediction of 3-D temperature fields (see Sect. 8.5.1).

While most observations are sensitive to atmospheric temperatures, either explicitly in the thermal range or just from the variation of line-strengths/cross sections in the solar reflected range (see Table 8.1), results remain partial and to some extent contradictory, despite significant progress in the last two decades. Part of the discrepancy is likely related to the fact that so far individual observations have reported a single "temperature" number, which must reflect some weighted means of altitude—and spatially—varying atmospheric temperatures. In principle, multi-transition observations in the thermal range would allow one to reconstruct a vertical temperature profile, as illustrated by the contribution functions for the rotational lines of SO_2 observed by the Atacama Large (sub)Millimeter Array (ALMA) (de Pater et al. 2020b). While the mm-wave data may, in principle, provide the best vertically-resolved constraints on Io's atmospheric profile, it has not yet been possible to determine a temperature profile, or even a representative temperature for the lower atmosphere probed at mm-wavelengths. As mentioned in Sect. 8.2.1, data interpretation is complicated by the additional effect of global winds or plume dynamics on the lineshapes, and the various geometries/lines-of-sight through the atmosphere and plumes with different temperature regimes, as illustrated in Fig. 8.2. As a likely consequence, even though the initial interpretations calling for ~600 K temperatures in the lower few scale heights (Lellouch et al. 1992) are now discarded, temperatures reported from recent mm-observations still range from ~150 K up to 320 K (e.g., Moullet et al. 2010; Roth et al. 2020; de Pater et al. 2020b). Using a high-energy line (580 K lower energy level), Lellouch et al. (2003) inferred $T = 180 \pm 60$ K from disk-average data; it is highly desirable to extend this approach to high angular resolution data.

The range of above temperatures is also generally consistent with UV constraints, that typically favor T = 200–300 K based on the shape of spectrally-resolved UV features (e.g. McGrath et al. 2000). In the infrared, Lellouch et al. (2015) used the structure of the $\nu_1 + \nu_3$ band at 4.0 μm in disk-resolved observations to infer a 170 ± 20 K mean gas temperature (Fig. 8.3). On the other hand, at 19 μm, the shape of the ν_2 band in disk-averaged spectra consistently indicates temperatures below 150 K (Spencer et al. 2005), with best determined temperatures on the anti-Jovian hemisphere (where SO_2 gas abundance is highest) of 108 ± 18 K (Tsang et al. 2012), as illustrated in Figs. 8.4 and 8.5. The contradiction between the two infrared results is puzzling as in a sense both are equivalent to direct rotational temperature measurements. In fact, a gas temperature as low as 108 ± 18 K is not obviously consistent with mm-wave line contrasts of 20–40 K above a ~95 K continuum. We note however that the anti-Jovian hemisphere has not been probed by either mm or 4.0 μm data, and that the association of colder lower atmospheric temperatures with higher columns is, at least qualitatively, predicted by models (Strobel et al. 1994; Walker et al. 2012) in which the lower atmosphere is shielded from plasma heating.

We further expect the temperature profile to vary with latitude, longitude, and time of day. Walker et al. (2012) developed a 3D model for a sublimation

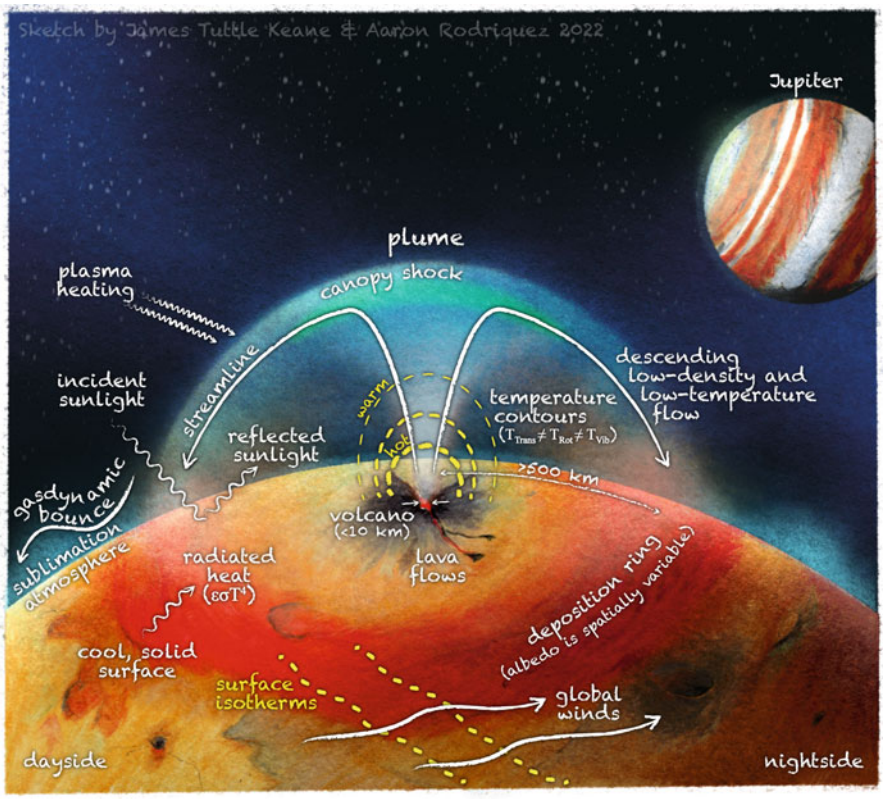

Fig. 8.2 Schematic drawing illustrating some of the complexity involved in interpreting remote observations of volcanic plumes. The drawing shows the plume with the warm high-density canopy at the top, the (white) streamlines, and several (yellow dashed) temperature contours, highest near the magma source. These temperatures include various levels of thermodynamic non-equilibrium (i.e., the translational, rotational and vibrational temperatures are not equal). The volcanic flow will interact with global winds triggered by the temperature distribution at the surface (indicated by the isotherms). The gas and particulate density is expected to be highest in the stem of the plume and the canopy, while, due to the non-equilibrium nature of the system as a whole, the distribution of gas opacity and emission at the various wavelengths is hard to predict. The particulate material falls down to the surface just inside the streamlines and the deposition ring. The temperature of the atmosphere is high where the downward flow "hits" the sublimation atmosphere (the light reddish color). Although spectral resolution may be excellent, the spatial resolution of observations is quite limited. Hence, what one "sees" notably depends on viewing geometry (e.g., view the plumes from any angle from nadir (straight down the plume axis) to large angles if portions of a plume are viewed beyond Io's limb) and whether one can view—or exclude from view—particular features. Illustration by James Tuttle Keane and Aaron Rodriguez

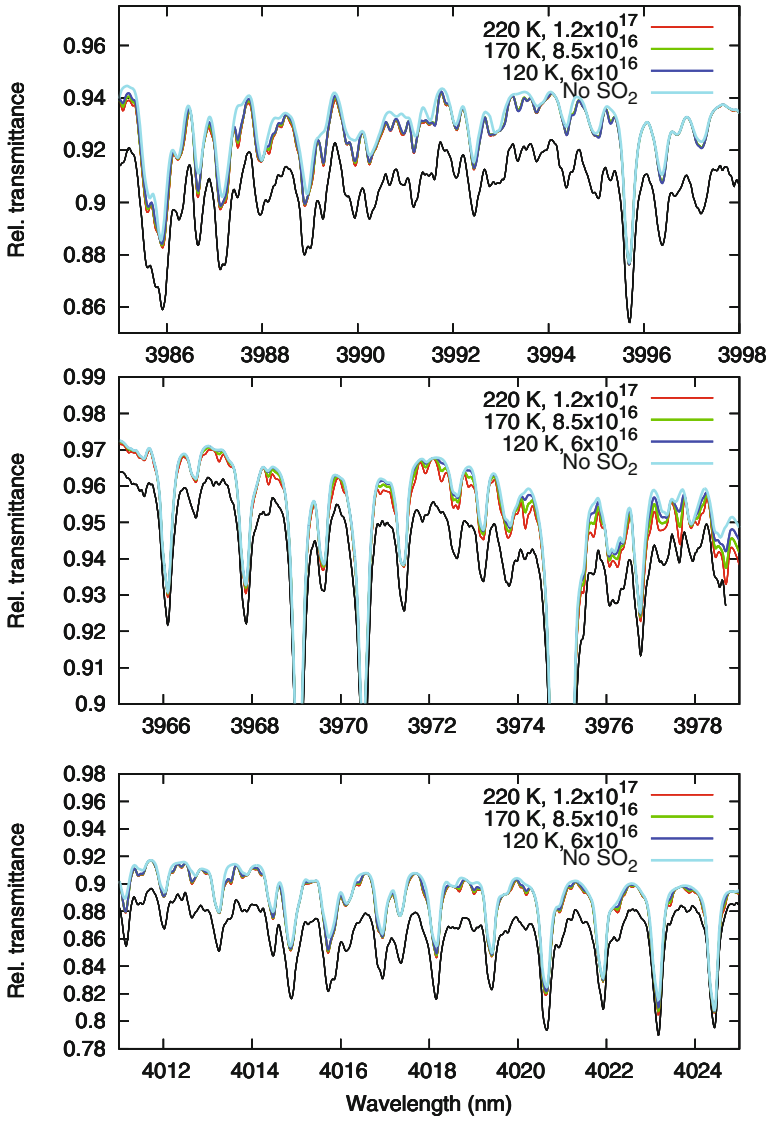

Fig. 8.3 Model fits to Io's reflected intensity at 4 μm. Observations are shown in black. Light blue: model without SO_2 gas. Red, green and dark blue lines show models with gas temperatures of 220, 170 and 120 K, respectively. Top panel: 3985–3998 nm. For each temperature, the SO_2 column density is adjusted to fit the spectrum in this wavelength range. These models are then compared to data at 3966–3978 nm (middle panel) and 4011–4024 nm (bottom panel). The best overall fit is obtained for T = 170 K. All model spectra are offset from the data (from Lellouch et al. 2015)

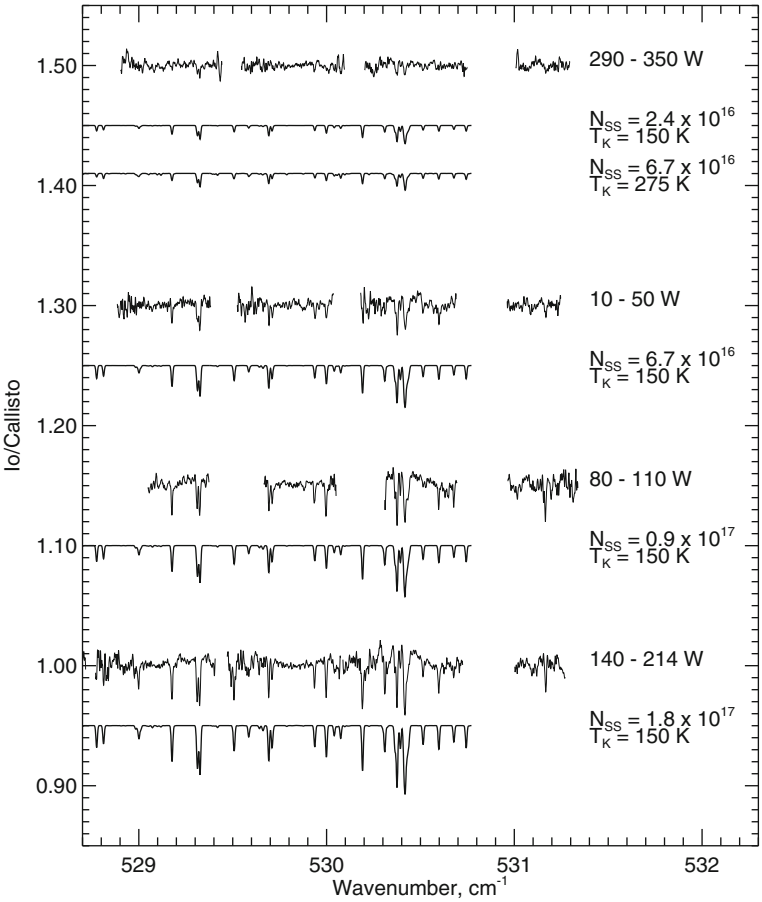

Fig. 8.4 Spectra of the ν_2 vibrational band at 19 μm, combined over several years and averaged by longitude, compared to disk-integrated models with similar line strengths (i.e., these models are not formal fits to the data). For the weakest lines, at 290°–350°W, two quite different models are shown that both match the spectral shape. This illustrates the ambiguity in interpreting some of the spectra. We further note that undulations in the continuum level are not real (from Spencer et al. 2005)

atmosphere to capture these variations and, like Strobel et al. (1994), suggest the presence of a layered thermal structure rather than an isothermal dayside atmosphere. In addition to this sublimation atmosphere with its longitudinal and latitudinal temperature variations, volcanic plumes affect the atmospheric structure (e.g., it is not hydrostatic around plumes) and temperatures dramatically (Sect. 8.4). Hence it is perhaps not surprising that disk-integrated observations at different wavelengths, likely probing different regions in the atmosphere and seeing plumes and the atmosphere as a whole under different viewing geometries (Fig. 8.2),

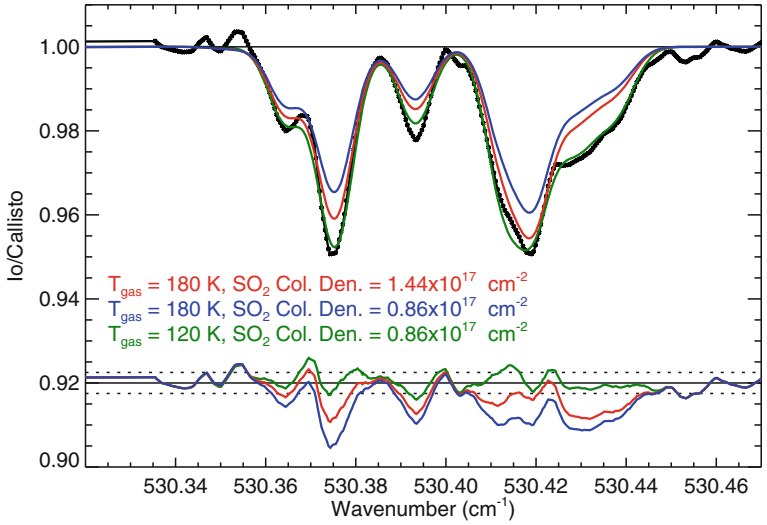

Fig. 8.5 Sensitivity of the 530.43 cm^{-1} wing of the ν_2 19-μm vibrational band to the kinetic temperature of the gas. The observations (black) are compared with synthetic spectra generated at (1) high gas temperatures, low SO_2 abundances (blue), (2) high gas temperatures, high SO_2 abundances (red) and (3) low gas temperatures with low abundances (green). The residuals are plotted at the bottom, offset to 0.92. The dotted lines show the noise level of the data. Although the high gas temperature, high abundance model spectrum fits reasonably well at the shorter wavenumbers, the 530.42 cm^{-1} line is poorly fitted. The lower gas temperature with the low abundance spectrum does match the observed spectrum much better (from Tsang et al. 2012)

give different results from atmospheric models assumed to be isothermal and in hydrostatic equilibrium.

Finally, poorly characterized and assumed isothermal temperature profiles may be the reason for the apparently anomalous $^{34}S/^{32}S$ ratio (2 times higher than terrestrial) derived from $^{32}SO_2$ and $^{34}SO_2$ mm lines (Moullet et al. 2013), since lines of the two isotopic variants have substantially different opacities and therefore probe different atmospheric levels.

8.3 Spatial Distribution and Temporal Variability of Io's Atmosphere

Despite a large observational body of work in the 1990s, it has been difficult to disentangle geographical variations, i.e., "organized" (i.e. diurnal, annual...) from "erratic" (i.e. related to unpredictable volcanic activity) time variations of Io's atmosphere. This dilemma lies at the core of the historic question of the primary source/driver of Io's atmosphere, a question we address in detail in Sect. 8.5.

In the present section we discuss the recent advances on the spatial distribution of the various gases, and their evolution with heliocentric distance and eclipse ingress/egress.

8.3.1 Dayside Atmosphere

Since the 1990s, using in particular new datasets in the UV and thermal IR, a consistent picture of the spatial distribution in Io's atmosphere has started to emerge. The SO_2 atmosphere consistently exhibits larger column densities on the anti-Jovian (180°W) hemisphere—of order $10^{17}\,cm^{-2}$ (though seasonally-variable, Sect. 8.5.1)—versus $\sim 10^{16}\,cm^{-2}$ at the sub-Jovian (0°W) hemisphere (e.g., Spencer et al. 2005; Feaga et al. 2009; Lellouch et al. 2015; Giono and Roth 2021). Millimeter-observations (Moullet et al. 2010, 2013; de Pater et al. 2020b; Roth et al. 2020) indicate typical values of $(0.7–2)\times10^{16}$ and at most $\sim 6 \times 10^{16}\,cm^{-2}$. However, except for the (near)-eclipse measurements of de Pater et al. (2020b) which sample the sub-Jovian hemisphere at 340°W and 20°W, the millimeter observations are typically focused on the leading (90°W) or trailing (270°W) hemisphere, and hence may miss the high anti-Jovian column densities ($\sim$1–1.5$\times10^{17}\,cm^{-2}$) seen at mid-infrared wavelengths. On timescales of a few months, repeated observations of Io's trailing side indicate modest variations ($\lesssim$30%) of the SO_2 columns, seemingly uncorrelated with hot spot activity (Roth et al. 2020).

The most detailed observational picture of the horizontal (latitude/longitude) distribution of SO_2 gas in Io's atmosphere is provided by the *HST*/Ly-α (121.6 nm) images over multiple years (Feaga et al. 2009; Giono and Roth 2021). Such images were first obtained in 1997 (Roessler et al. 1999), and revealed bright polar regions separated by a dark equator. It is now widely accepted that the equatorial region is dark because SO_2 in Io's atmosphere absorbs the surface-reflected solar Ly-α radiation (e.g., Feldman et al. 2000; Strobel and Wolven 2001), and since that time *HST*/Ly-α images have been instrumental in mapping SO_2 gas across Io's surface. The maps reveal that SO_2 gas is mainly confined to latitudes within 30–40° from the equator, with a larger latitudinal extent on the anti-Jovian side, and maximum column densities of $\sim5 \times 10^{16}\,cm^{-2}$, i.e., intermediate between the mm and 19-μm values, reached at $\sim$140°W on the equator (Feaga et al. 2009). In a recent paper, Giono and Roth (2021) show that these Ly-α images are only sensitive to SO_2 column densities between $\sim10^{15}$ and $5\times10^{16}\,cm^{-2}$ due to a strong non-linearity in the relationship between SO_2 abundance and Ly-α flux. Based upon a statistical analysis, they show that the maximum SO_2 abundances in the images are closer to $\sim10^{17}\,cm^{-2}$ (Fig. 8.6), i.e. in agreement with mid-infrared results. The drop in column density towards the higher latitudes is interpreted as due to condensation of SO_2 closer to the poles. Attempts have been made to use this observed spatial geographical distribution to constrain the sublimation vs volcanic nature of Io's atmosphere, but with limited success (see Sect. 8.5.1). ALMA maps of the SO_2

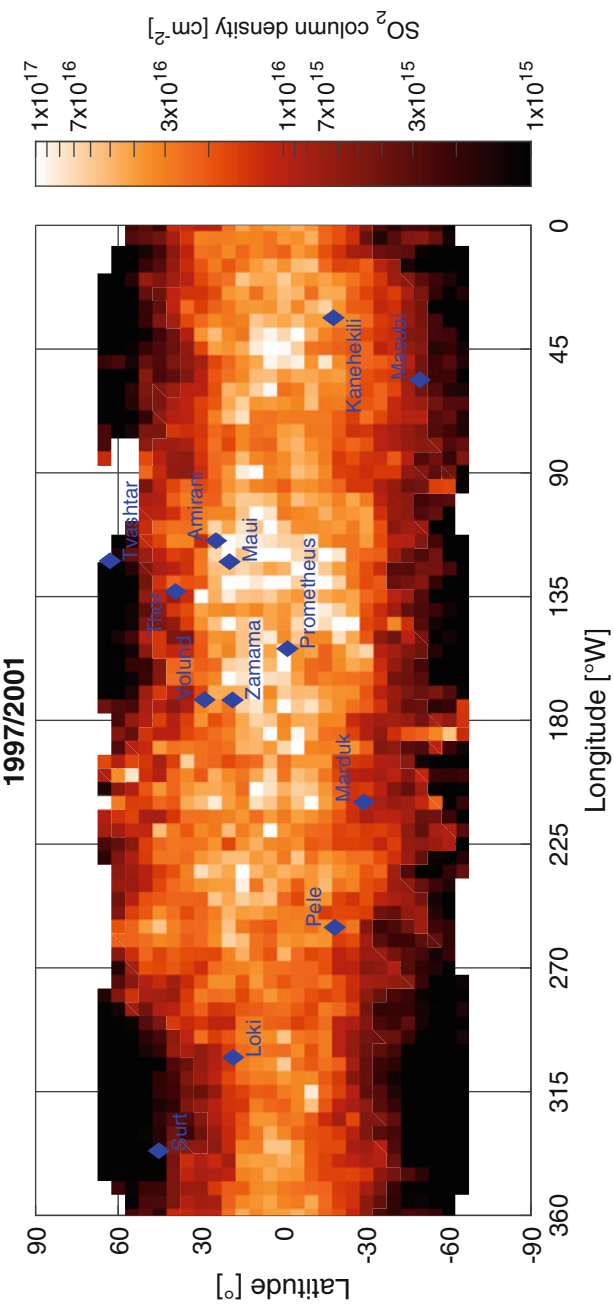

Fig. 8.6 The SO_2 spatial distribution as derived from multiple years of far-UV data obtained with *HST*/STIS. The cylindrical projection shows the obvious difference in abundance between anti- and sub-Jovian hemispheres. Column densities are displayed on a logarithmic color scale (from Giono and Roth 2021)

emission at mm-wavelengths, discussed in Sect. 8.3.2, also show the emissions largely confined to latitudes within 30–40° from the equator (de Pater et al. 2020b).

The spatial distribution of atmospheric gases is also affected by active volcanoes. Most volcanic hot spots as observed at near-infrared wavelengths are at mid-latitudes, with maxima in the number of hot spots near longitudes of ∼330° and ∼150°, and a relative lack right at equatorial latitudes. Although the number of hot spots is similar between the leading and trailing hemispheres, bright transient eruptions usually take place on the trailing hemisphere (de Kleer et al. 2019a) and at preferentially higher latitudes (de Kleer and de Pater 2016b; Cantrall et al. 2018). At least some of these transient eruptions have been associated with active plumes (e.g., at Tvashtar Patera in the far north, Sect. 8.4.1), but since the plumes themselves cannot be detected at the infrared wavelengths used to map the distribution of hot spots, it is usually not known if a hot spot is connected with a plume. The best way to detect plumes is either from spacecraft or *HST* in the UV (Sect. 8.4.1), or during an eclipse (Sects. 8.3.2 and 8.3.3).

8.3.2 Eclipse Response

The evolution of molecular and atomic emissions before, during and right after an eclipse provides a diagnostic tool to investigate the sources and stability of Io's atmosphere. Io's atmosphere is unique in this aspect; no other body is subject to such periodic, huge impulse responses. As soon as the satellite enters an eclipse, the atmospheric and surface temperatures drop, and SO_2 is expected to condense out on a time scale possibly as short as ∼70 s (Sect. 8.2.2). This process proceeds from the bottom up: i.e., SO_2 condenses onto the cold surface, destabilizing the atmosphere, so that the gas above it falls down since it is no longer supported from below. Hence, the atmosphere collapses, as illustrated by the solid line in Fig. 8.7. If, however, non-condensible gases are present, as indicated by the dashed line in Fig. 8.7, one may not expect a total collapse of the atmosphere (Moore et al. 2009). In that case, the non-condensible gas rapidly forms a layer along the surface through which the condensing SO_2 must diffuse, perhaps greatly delaying collapse even of the condensible component. During this process the lower atmosphere can warm both due to the recovery of the potential energy of falling gas (compression) as well as the ready penetration of warming plasma nearly to the surface.

The process described above is not symmetric during ingress/egress because the SO_2 subliming off the suddenly warmed surface upon egress can simply lift the non-condensible gas off the ground. In fact, detailed solutions of the Boltzmann equation for this entire ingress/egress scenario indicate the possibility of numerous vertically propagating waves associated with the atmospheric bounce as it responds to an abrupt change in surface boundary condition (Kosuge et al. 2012).

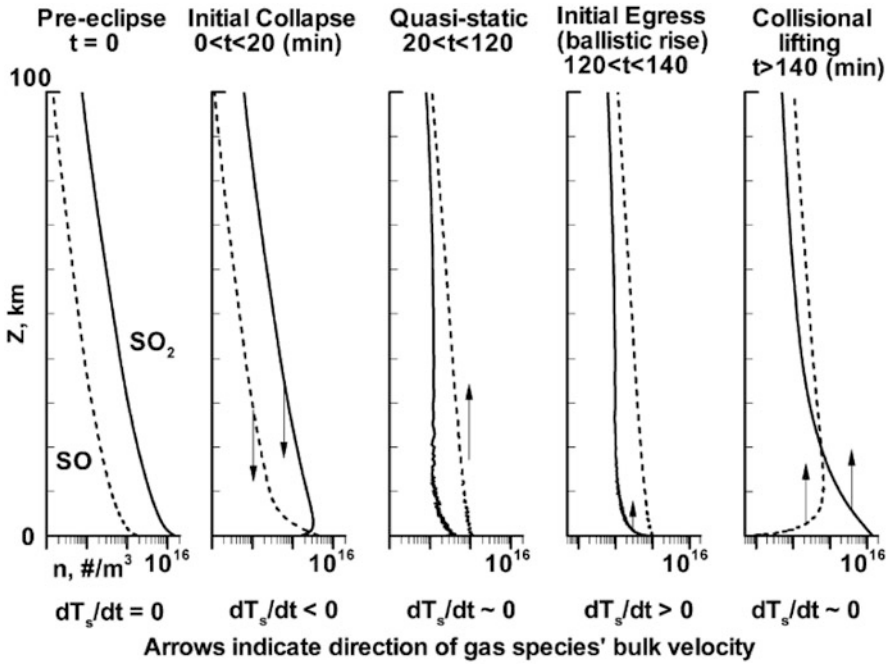

Fig. 8.7 Schematic of the atmospheric dynamics starting before eclipse (left-most panel), through eclipse ingress and until after egress. The altitude is shown on a linear scale on the vertical axis up to 100 km and the number density is shown on a log scale from 10^{13} to $2 \times 10^{16}\,\mathrm{m}^{-3}$. The solid lines represent SO_2 and the dashed lines the SO (or any other non-condensible gas) number density. Several distinct periods (labeled at the top) occur during eclipse and early egress and are shown from left to right (From Moore et al. 2009)

8.3.2.1 SO_2 Observations

From an Earth-centered observational point of view, eclipses occur when the sub-Jovian hemisphere is in view, with eclipse ingress (resp. egress) occurring near 340°W (resp. 20°W). The first direct observations of a near-collapse of atmospheric SO_2 when Io entered an eclipse were obtained by Tsang et al. (2016) at a wavelength of 19 μm with the TEXES instrument on the Gemini telescope. They measured a drop in surface temperature from 127 to 105 K within minutes after entering eclipse (Fig. 8.8a). Using different atmospheric cooling models, the analysis of the decrease in band depth from 2.5% down to ~0.2% was interpreted as a decrease in the SO_2 column density by a factor of 5 ± 2 (down from $\sim 2\text{-}2.5 \times 10^{16}\,\mathrm{cm}^{-2}$). In contrast, though, Tsang et al. (2015) did not see any change at UV wavelengths when Io went from eclipse into sunlight on two dates in 2011, which was attributed to a larger number of active volcanoes near the egress longitudes compared to ingress (Tsang et al. 2016). However, the UV data were averaged over 10 min time intervals, and on the second day observations did not start until 10 min after egress. As shown

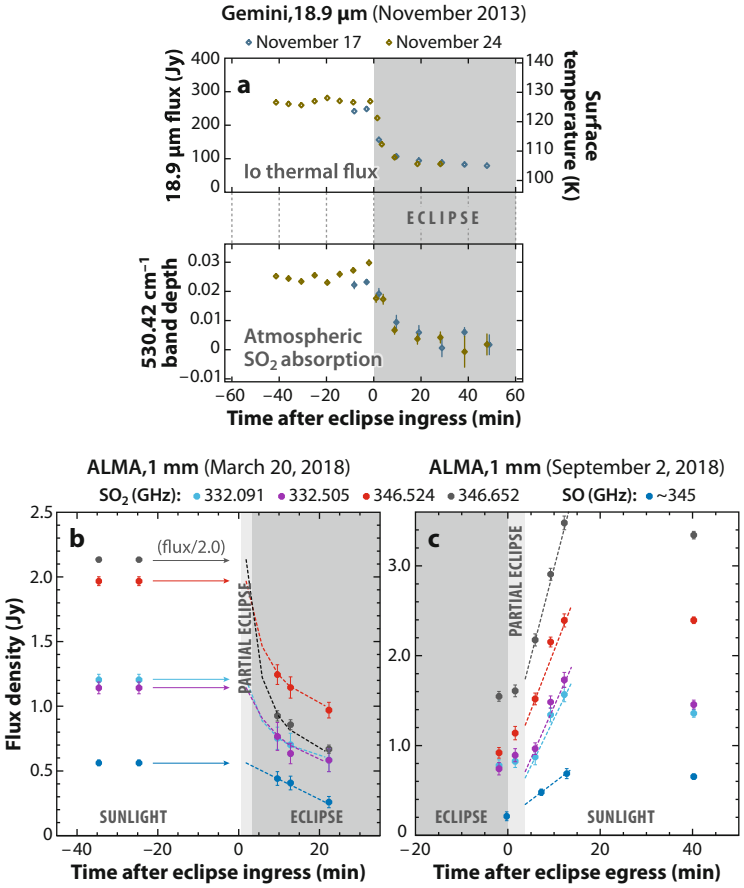

Fig. 8.8 Observations of Io going into and emerging from eclipse. (**a**) Gemini data at 19 μm: (top) The thermal flux of Io and (bottom) the SO_2 absorption depth at 530.42 cm^{-1} in 2013 on Nov. 17 and 24 as a function of time relative to eclipse ingress (Tsang et al. 2016). (**b**, **c**) ALMA data at 1 mm: SO_2 and SO disk-integrated flux densities (from maps integrated over 0.4 km/s, centered on the line) are plotted as a function of time for eclipse ingress (panel **b**) and egress (panel **c**). The dotted lines superposed on the data in panel (**b**) show the exponential decrease in the first few minutes after entering eclipse. In panel (**c**) the dotted lines show the linear increase after emerging from eclipse on September 2. The flux density of the 346.652 GHz data in panel b is divided by a factor of 2. All data are normalized to a geocentric distance of 5.044 AU (de Pater et al. 2020b). Figure reproduced from de Pater et al. (2021)

below, the atmosphere reforms within 10 min after eclipse egress, so we note that the UV observations may have just missed the low in-eclipse abundances right before eclipse egress.

Both eclipse ingress and egress were observed with ALMA in the 1-mm wavelength band (de Pater et al. 2020b). The evolution of the disk-integrated intensities in several transitions of SO_2 together with SO is shown in Fig. 8.8b,c. During eclipse

ingress, the SO_2 flux density dropped exponentially, but was re-established in a linear fashion within about 10 min of time after re-emerging in sunlight, with an extra up to ~20% "post-eclipse brightening" after ~10 min. This extra brightening may somehow result from the complex dynamics involved in the interaction of the plumes with the reforming atmosphere (Sects. 8.4.3 and 8.5.2; de Pater et al. 2020b). Disk-integrated in-sunlight flux densities are ~2–3 times higher than in-eclipse, indicative of a roughly 30–50% contribution from volcanic sources, unless the presence of non-condensible gases prevents complete atmospheric collapse as in Fig. 8.7 (Moore et al. 2009), or plasma from the torus, which can now reach parts of the surface, contributes to the atmosphere via surface sputtering.

Maps of Io's emission during eclipse ingress and egress, shown in Fig. 8.9, show an overall collapse of the atmosphere, except for emissions near the known volcanic sites Karei Patera, Daedalus Patera, and North Lerna during ingress, and P207 patera just before egress. The latter is a small visibly dark patera; plumes have never been reported at this site. As soon as sunlight hits the satellite during egress, SO_2 emissions become stronger in particular in the regions where volcanic plumes were present during eclipse, and after ~10 min the SO_2 atmosphere has completely reformed (de Pater et al. 2020b).

Surprisingly, the SO_2 column density (1.5×10^{16} cm^{-2}) and temperature (~270 K), derived from disk-integrated flux densities under the assumption of an atmosphere in hydrostatic equilibrium, appear to be essentially the same both for the Io-in-sunlight and in-eclipse data; the difference can be explained entirely by a factor of 2–3 decrease in fractional coverage over the disk when in-eclipse (de Pater et al. 2020b). These findings may agree with the factor-of-5 drop in column density at mid-infrared data as reported by Tsang et al. (2016), since they cannot distinguish between a high column density with low fractional coverage and a low column density with a high fractional coverage. Similar results were typically obtained for individual plumes, where the fractional coverage within a beam centered on the plume decreased by a factor of 2–3 when going into eclipse, while the column density and temperature stayed more or less the same (de Pater et al. 2020b). The authors stressed, however, that the models used to fit the data were hydrostatic models, and during an eclipse and in plumes the applicability of such models is very limited.

The ALMA maps can be compared with the DSMC simulations for a purely sublimation-sourced atmosphere before/during/after eclipse (Walker et al. 2012), shown in Fig. 8.10. These simulations are based on a parametric study of Io's thermophysical surface properties, using three thermal units: (1) frosts/ices with surface areas as in Douté et al. (2001), with a best-fit albedo A = 0.55 and thermal inertia $\Gamma = 200$ J m^{-2} K^{-1} s$^{-1/2}$ (hereafter referred to as MKS units), (2) non-frosts with A = 0.49, $\Gamma = 20$ MKS, and (3) hot spots. The thermophysical properties were derived by fitting the model to observations at mid- to near-UV wavelengths, and assuming that the column density must be in vapor pressure equilibrium with the surface temperature. The modeled images are centered at 10°N, 350°W, and show the predicted changes over time from ~2 h before local noon to ~4.5 (Earth) h later, with an eclipse in between. The subsolar point is indicated by the white

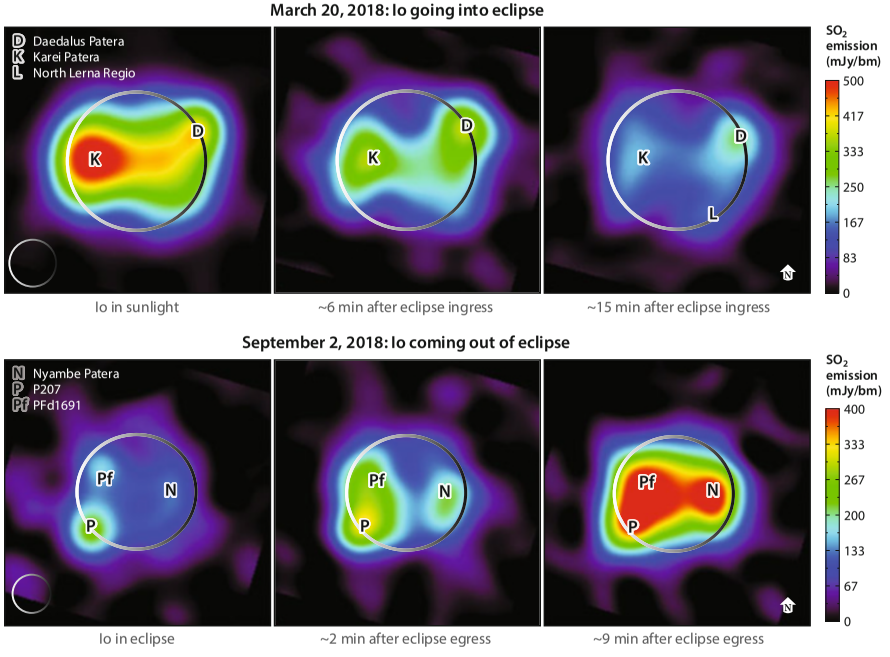

Fig. 8.9 Individual frames of a series of ALMA SO_2 maps constructed from data at 346.652 GHz when Io went into eclipse (20 March 2018) and emerged from eclipse (2 September 2018). The data are averaged over 0.4 km/s (~0.45 MHz). The large circle shows the limb of Io, and the small circle in the lower left shows the resolution of the data (0.35″ or 1205 km in March; 0.30″ or 1235 km in September). The effect of volcanoes on Io's SO_2 emission is clearly seen (de Pater et al. 2020b). Figure reproduced from de Pater et al. (2021)

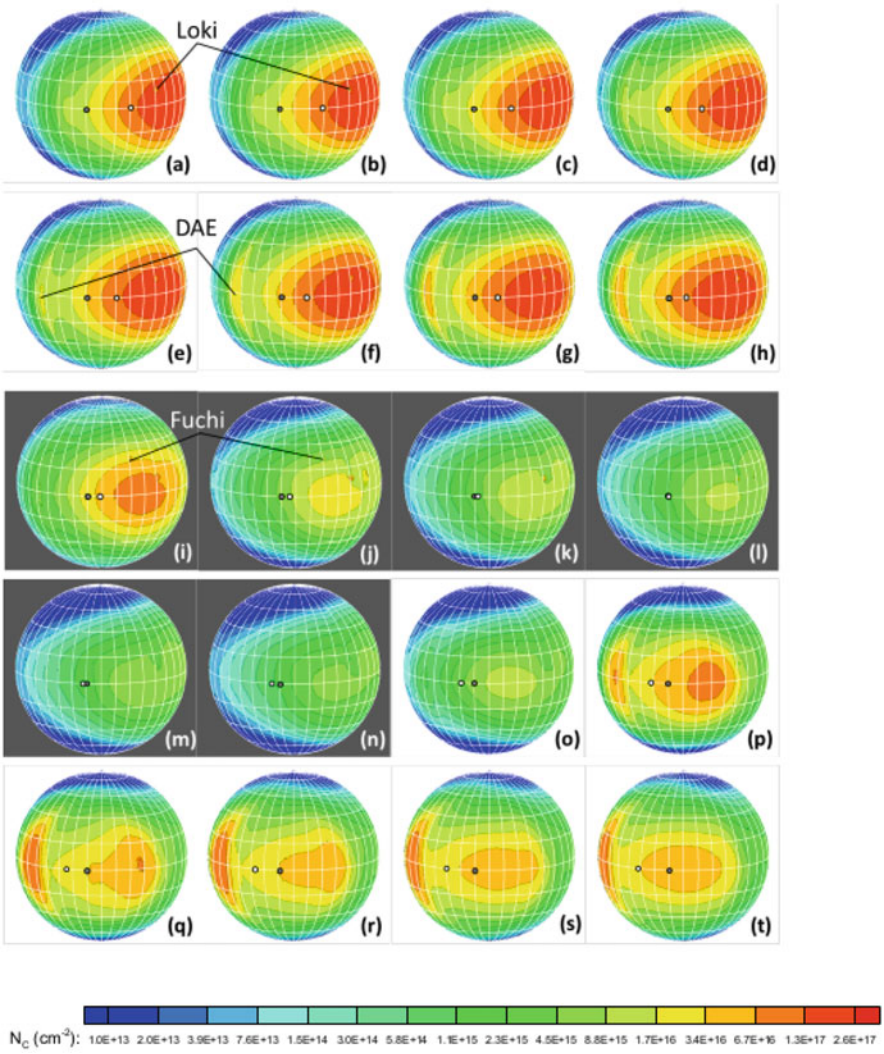

Fig. 8.10 Column density contours with a view centered at 10°N, 350°W as a function of time. The 20 snapshots at intervals of 1250 s starting approximately 2 h and 40 min prior to eclipse and ending ~ 2 h after egress from eclipse. Hence the first in-eclipse panel is 6.7 min after eclipse ingress, and the first panel upon egress is taken after Io was 11 min in sunlight. So they correspond to the top middle and lower right panels in Fig. 8.9. Two hot spots (Loki Patera and Fuchi Patera) are highlighted in (a), (b), (i) and (j). The white dot denotes the location of the subsolar point while the black dot denotes the sub-Jovian point. DAE refers to the dawn atmospheric enhancement (From Walker et al. 2012)

dot, and moves across the satellite from sunrise to sunset. In contrast, Earth-based observations show Io rotate over time, while the subearth and subsolar point remain fixed near the center of Io.

Despite these differences in geometries, the ALMA and DSMC results both trend toward an equatorial confinement of SO_2 outside of eclipse due to condensation of SO_2 at the higher colder latitudes. During eclipse, both ALMA and DSMC results show a decrease in the disk-integrated flux density, followed by a recovery upon egress, if we use the modeled column density as a proxy for flux density. The flux density in the ALMA data changes much faster, however, both upon ingress and egress than the models show. Moreover, the structure shown in the ALMA maps, apart from the equatorial confinement, appears to be dominated by the presence of volcanic plumes, whereas the bimodality in the modeled column density before and after eclipse arises largely from the presence of an atmospheric enhancement at dawn (DAE) coupled to the adopted distribution of frost coverage on the surface, i.e., the DAE is located over a low thermal inertia region ($\Gamma = 20$); the SO_2 gas, once released from the surface shortly after sunrise, will move towards lower pressures and condense if/when meeting lower surface temperatures, such as at night, at higher latitudes, and above SO_2 still-cool frost along the equator. Hence this feature depends much on the spatial distribution of frost and bare rock in the models; there is, as of yet, no clear evidence of DAE in the data. Clearly, there are a number differences between data and models that need to be reconciled in future work (see Sect. 8.5 for more discussion).

8.3.2.2 SO Observations

Despite the fact that SO, as a non-condensible gas, is not expected to significantly condense during an eclipse (Sect. 8.2.2), Fig. 8.8 shows a gradual (linear) decrease in the SO flux density by a factor of ~2 upon eclipse ingress. ALMA maps of SO (not shown here) during eclipse-ingress look very similar to the SO_2 maps in Fig. 8.9, but with a delayed response as in Fig. 8.8. Since SO had not been thought to experience condensation, it may be removed from the atmosphere through reactions with itself on the surface at a much faster rate than anticipated (de Pater et al. 2020b). The chemical reaction rate may be increased due to an increase in the SO partial pressure at the surface, because SO is forced into a thin layer by the collapsing SO_2 column of gas, which increases the collision rate of SO molecules in the atmosphere and with the surface. Some SO may also get trapped in porous surface layers through this process. Upon eclipse egress, SO is restored about three times more slowly than SO_2, as expected if SO is formed primarily through photolysis (de Pater et al. 2020b), perhaps augmented by a slow release from the surface.

SO has also been observed and mapped while in eclipse at near-infrared wavelengths. Such SO emissions were first detected in 1999 at 1.707 μm (de Pater et al. 2002). They were attributed to the SO forbidden electronic $a^1\Delta \rightarrow X^3\Sigma^-$ transition, and these first disk-integrated measurements were indicative of a rotational temperature of ~1000 K. The authors hypothesized the emissions to

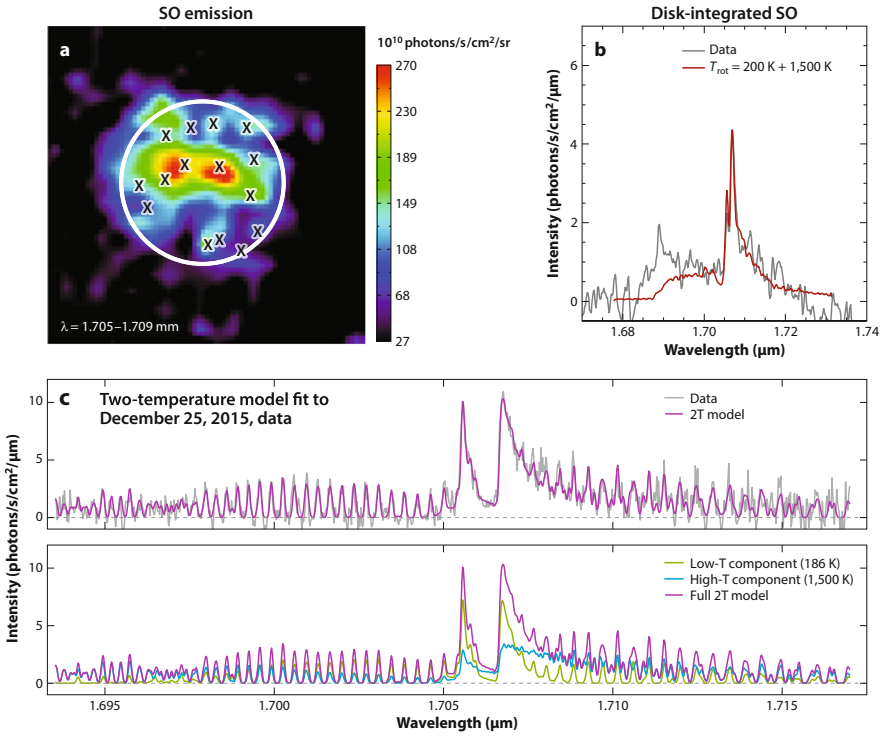

Fig. 8.11 (**a**) Keck image of the forbidden 1.707 μm emission band of SO obtained with the field-integral spectrometer OSIRIS on the Keck 2 telescope on 25 Dec. 2015. The image is obtained by integrating over the center channels of the emission band (see panel (**b**)). Superposed are the location of a number of volcanic centers (note the absence of a clear one-on-one correlation), and the limb of Io's disk. (**b**) Disk-integrated OSIRIS spectrum of the SO data in panel a, with a model consisting of two temperatures (200 and 1500 K, in approximately equal proportions) superposed. Note that the 1.69 μm feature cannot be matched. (**c**) Disk-integrated spectrum at a high spectral resolving power (R ~ 25,000) taken simultaneously with the data in panels (**a**) and (**b**). A very similar 2-temperature model is superposed. The individual components of the model are shown in the bottom panel (panels a,b from de Pater et al. 2020a) (panel c from de Kleer et al. 2019b). Figure reproduced from de Pater et al. (2021)

originate at Loki Patera, which was exceptionally bright in the near-infrared at the time. They discussed many potential explanations, including the electron impact mechanism which causes the auroral glows on Io (Sect. 8.3.3), and concluded that the SO emission must result from excited SO molecules directly ejected from the vent at a thermodynamic quenching temperature of ~1500 K.

More recent observations at a higher spectral resolution (Fig. 8.11c) indicate the presence of gas at both a low (~200 K) and high (~1500 K) temperature (de Kleer et al. 2019b). This combination is required to fit the detailed band shape over 1.695–1.715 μm (Fig. 8.11c), but the interpretation of these two temperatures is uncertain. Furthermore a secondary emission at 1.69 μm remains unexplained (Fig. 8.11b),

suggestive of poorly understood non-LTE effects, such as expected in gas dynamic plumes. Most relevant for the origin of this emission, the spatial distribution of SO as derived from Keck/OSIRIS measurements (Fig. 8.11a) shows that the correlation with known volcanoes is tenuous at best, leading de Pater et al. (2020a) to suggest that the emissions are likely caused by a large number of "stealth" plumes (See Sect. 8.4.2).

8.3.3 Auroral Emissions

Galileo images of Io while in eclipse showed a colorful display of red, green, and bluish glows attributed to atomic and molecular emissions excited via electron impact (e.g., Geissler et al. 1999). Subsequent spacecraft and *HST* images (e.g., Geissler et al. 2001, 2004a; Roth et al. 2014) revealed a complex morphology of these glows, as shown in Fig. 8.12: (1) equatorial "spots", one on either side of Io's disk, usually referred to as Io's "aurora"; (2) bluish glows from volcanic plumes; (3) a reddish ring of emission surrounding the entire disk; (4) faint glows across parts of Io's disk; *v*) emissions have also been seen from Io's extended corona, out to ∼10 R_{Io}. While emissions have been reported, indirectly, from Io's plasma wake (e.g., Retherford et al. 2007), such emissions have not been confirmed (e.g., Roth et al. 2014).

The equatorial spots rock back-and-forth about the equator as seen on the sky in response to the changing orientation of Jupiter's magnetic field. The spots track the tangent points of the Jovian magnetic field lines with Io, and are produced by electrons impacting the various atmospheric gases. Most of these emissions originate within 100 km from the surface, and the variations can be explained by a combination of the local plasma environment and the changing viewing geometry of Io in Jupiter's magnetosphere (e.g., Roth et al. 2014).

Spectra of the emissions, obtained primarily from *HST*/STIS observations, yield information on the composition and abundance of these glowing gases, and the intensity of the electrical currents that excite the emissions (e.g., Geissler et al. 2004a; Trafton et al. 2012; Roth et al. 2014). The bluish glows from aurora and volcanic plumes are dominated by emissions from molecular SO_2. Some of the atomic species, e.g., O, Na, and K, produce line emissions at longer visible and near-infrared wavelengths, resulting in more reddish glows. These glows, which are brighter on the side of Io closest to the center of the plasma torus, surround the entire disk (the limb glows), and hence indicate that these species (O, Na, K) are spread across Io's surface and are not only confined to the equatorial regions, in contrast to the near-equatorial distribution of SO_2 gas, which condenses at the colder higher latitudes, as discussed above.

Since the auroral emissions depend on the column density of the emitting species as well as the impinging electron flux and temperature, the latter of which is controlled by the penetration depth into the atmosphere of the impacting electrons (the electrons, originating in the plasma torus, cool after entering the atmosphere),

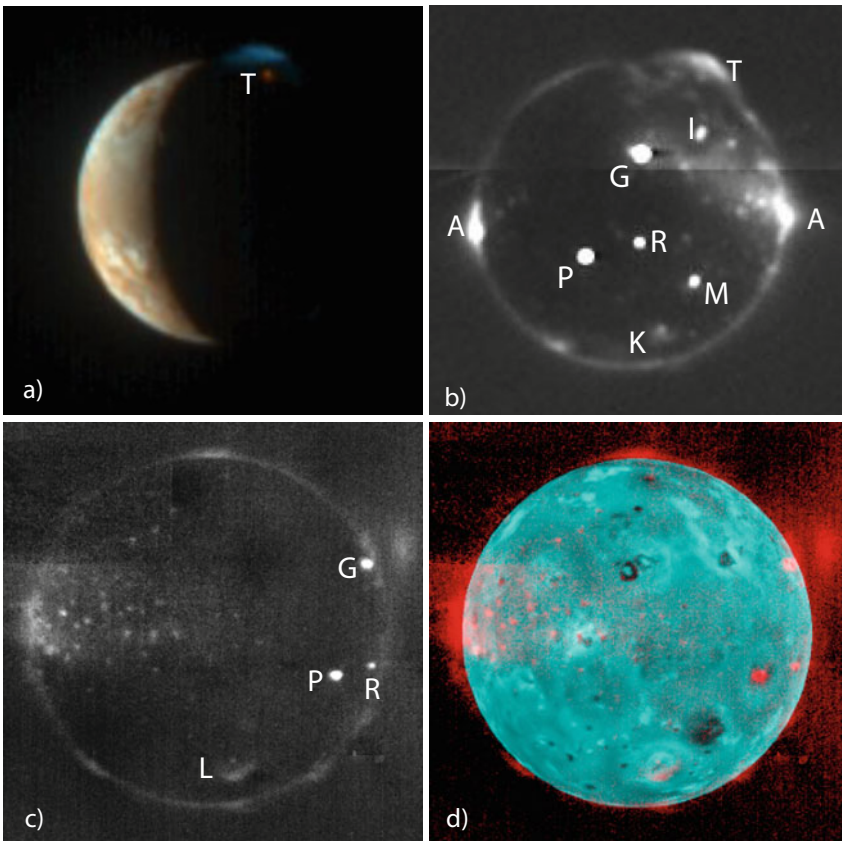

Fig. 8.12 (**a**) Nighttime glow of the north-polar Tvashtar volcano (T) and its plume rising 330 km above Io's surface. This image was taken with the blue and methane filters of the Multispectral Visible Imaging Camera (MVIC) of the imaging instrument Ralph on the *New Horizons* spacecraft on March 1, 2007. The image shows an intense red color (methane-band image) of the glowing lava at the plume source, and the contrasting blue (blue-filter) of the fine dust particles in the plume. The lower part of the plume is in Io's shadow, and hardly visible in this image. (**b**, **c**) *New Horizons* images of Io-in-eclipse. The brightest spots on the disk are "hot spots", thermal emissions from hot lava at active volcanoes. The brightest spots are indicated: P: Pele, R: Reiden Patera, M: Marduk Fluctus, G: East Girru Patera, I: Isum Patera. A plume is seen over a hot spot at N. Lerna (L) in panel (**c**), and over Kurdalagon Patera (K) in panel (**b**). The plume above Tvashtar (T) rises out above the limb in panel (**b**) (Tvashtar itself is not visible; it is just over the limb). Diffuse glows and faint spots are from gas in the plumes and atmosphere. On either side of the satellite, along the equator, are auroral spots (A), where the eastern spot might be enhanced by the Prometheus plume, and the western one by Ra Patera, which are both right on the limb. The edge of Io's disk is outlined by a faint glow. (**d**) The eclipse image from panel (**c**) (in red) overlain on a sunlit image (cyan). The numerous point-like sources near the equator in both (**b**), (**c**) might be manifestations of stealth volcanism (PIA09254, PIA09354, PIA10100) (NASA/JHU/APL/SwRI)

the change in emissions during an eclipse provide information on the sources and losses of the emitting gases, as well as changes in the atmospheric density. Disk-averaged observations of Io have shown a factor-of-3 decrease in the far-UV atomic S and O emissions ~20 min. after eclipse ingress (Clarke et al. 1994), and a factor-of-2 increase after egress (Wolven et al. 2001). Sodium emissions decreased by a factor-of-4 during eclipse ingress, and recovered after egress (Grava et al. 2014). Most of the changes in auroral glows happened in the equatorial spots, while the limb glow and extended corona did not seem to change much (Retherford 2002). Hence one might attribute a decrease in these aurora to a (temporary) "break" in the production rate. Indeed, the decrease in S, O, and Na glows have been attributed to a lack of photodissociation (from SO_2 and NaCl) when the satellite is in Jupiter's shadow.

Figure 8.13 shows two spectra, one taken during the first 14 min after eclipse ingress, and a second one averaged over the subsequent (almost) equal time period. The decrease in all emissions during the eclipse is clearly visible, indicative of ongoing atmospheric collapse due to freeze-out. In addition to these identified species (SI multiplets, SO, SO_2), there are unidentified emissions between 0.33 and 0.57 μm, seemingly caused by a tri-atomic molecule like SO_2, S_2O, or perhaps

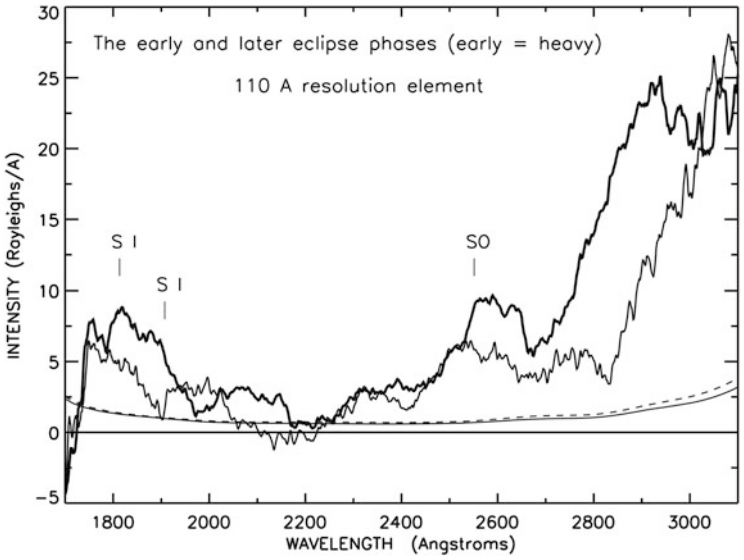

Fig. 8.13 Change in spectra during an eclipse, as observed with the MAMA UV (0.175–0.320 μm) detector of *HST*/STIS on August 18, 1999. The heavy line shows the spectrum as averaged over the first 14 min upon eclipse ingress; the thinner line shows a spectrum averaged over a time from 17 to 29 min after eclipse ingress. The curves near the bottom of the plot represent the 1-σ errors for the early (solid line) and later (dashed line) observations. The SI lines and SO are indicated; the broad SO_2 band rises to the right above 2200 Å across the plot (with SO superposed). The sharper rise on the right likely includes Io's attenuated continuum, which becomes weaker deeper into eclipse (and with declining UV wavelength) (Adapted from Trafton et al. 2012)

caused by positive or negative ions of SO_2 and its daughter species (Trafton et al. 2012). For these spectra, Trafton et al. (2012) showed that dissociative excitation of SO_2 by electrons in the plasma torus is a significant source of emission by its daughter products S and SO.

Saur and Strobel (2004) modeled the response of auroral emissions upon entering and exiting eclipse, assuming the emissions are caused by electrons from the (upstream, i.e., trailing hemisphere) plasma torus impacting the atmospheric gases. They assumed a column density of $1.5 \times 10^{16}\,\mathrm{cm}^{-2}$ before eclipse, and calculated the response in auroral emissions throughout atmospheric collapse. They showed that the auroral glows can only decrease in intensity, as observed for the equatorial spots, if the atmosphere collapses down to column densities <3–$5 \times 10^{14}\,\mathrm{cm}^{-2}$. At such low densities, the impacting electrons have kept their high plasma temperature ($\sim$5 eV), and emissions vary linearly with atmospheric column density. At atmospheric densities over $\sim 5 \times 10^{14}\,\mathrm{cm}^{-2}$, the auroral emissions will brighten upon eclipse ingress. A delay of the plasma interaction upon eclipse egress, when sublimation of surface frost increases the atmospheric density, may therefore result in a post-eclipse brightening in the UV. We note that whether the emissions dim or brighten is a very non-intuitive process, since the electron temperature affects the emissions in an extremely non-linear fashion, so that small changes in temperature can have large effects in the emissions. Also, the intensities of the emissions depend on the fraction of upstream Io torus flux tubes that intercept and feed energy into the atmosphere. This fraction is controlled by the strength of Io's electrodynamic interaction that depends on the ratio of the Alfvén conductance to the ionospheric conductances, adding further non-linearity to the auroral emissions' response. When modeling the aurora as observed with *New Horizons* when Io was in eclipse, Roth et al. (2011) derived an order of magnitude decrease in the atmospheric density compared to in-sunlight, in agreement with the above theory; their derived densities, however, were about two times higher than the $\sim 5 \times 10^{14}\,\mathrm{cm}^{-2}$ maximum value mentioned above for the equatorial spots, perhaps indicative of the complexity of the interaction.

In contrast to the aurora, plumes have been seen to brighten in eclipse (Geissler et al. 1999), which is caused by the same process discussed above: the background atmosphere is collapsing, but the plume column density is high. So any change may brighten the plume emissions, but certainly not dim it (Saur and Strobel 2004).

Several authors (e.g., Sauer et al. 2002; Roth et al. 2011; Dols et al. 2012; Blöcker et al. 2018) have modeled the magnetic field and plasma perturbations near Io to derive diagnostics on Io's atmosphere. In particular, they find a longitudinal asymmetry very similar to that derived from the UV and mid-IR data (Sect. 8.3.1). These simulations further suggest that the atmosphere's radial extension is limited upstream (scaleheight $\sim$60 km) and at least several times larger on the anti-Jovian downstream side, where simulations support a very extended corona ($\gtrsim 6\ R_{Io}$) of SO_2 and SO.

8.3.4 Atmospheric Escape

Although the source of Io's atmosphere can ultimately be attributed to volcanism, it must be continuously replenished since Io loses ∼1 ton/s (∼3×10^{28} atoms/s) of material to its neutral clouds and the magnetosphere, primarily through sputtering by ions in the plasma torus (e.g., Spencer and Schneider 1996). Most sputtered products, however, will have velocities much less than Io's escape speed of 2.6 km/s, and populate Io's corona or exosphere, out to the boundary of the satellite's Hill sphere (∼6 R_{Io}). Those that do have higher velocities form Io's neutral clouds. Other important processes that lead to a loss from Io's atmosphere (and its corona and neutral clouds) are electron impact ionization of an atmospheric atom by an electron from the plasma torus (electron impact on a molecule often leads to dissociation), and charge exchange between an atmospheric atom or molecule with an ion in the torus; upon ionization the new ions are accelerated and supply the plasma torus with fresh material, while the newly formed neutral will keep its high velocity and populate extended neutral clouds (e.g., Mendillo et al. 1990; Schneider and Bagenal 2007; See also Chap. 9 in this book). Given the inferred supply rates to the torus for O and S, the atmospheric lifetime is of order 10 days for a 1 nbar atmosphere covering 25% of the surface (Lellouch 1996).

Mendillo et al. (2004) had reported a positive correlation between Io's infrared brightness and the brightness of the extended sodium cloud, but an increase in Io's infrared brightness does not necessarily imply plume activity. Moreover, direct ejection of material from volcanoes should not be important, since the ejection speeds (at most ∼1 km/s) are well below Io's escape speed. McDoniel et al. (2019) show that the interaction of plasma from Io's plasma torus with volcanic plumes depends much on the location of the plume due to the direction of the impinging plasma. They show that, although plasma does inflate plume canopies, the rising plume itself is not much affected and the canopy height barely changes. A large, diffuse neutral cloud may form above the canopy, and some SO_2 and its dissociated daughter products may escape the plume and add material to Io's corona and exosphere. Upon ionization, these may escape Io's direct environment, and hence form a potential source of material for the plasma torus.

The Japan Aerospace Exploration Agency (JAXA) *Hisaki* satellite has been studying UV emissions from ions and neutrals in the Jovian system from Earth's orbit since 2013 (Yoshikawa et al. 2014). In January–March 2015, using a combination of groundbased telescopes and *Hisaki*, a brightening of Io's extended sodium cloud and plasma torus was observed (Tsuchiya at al. 2015; Yoneda et al. 2015), while Io's extended neutral oxygen cloud spread outward from Jupiter, with a more than doubling of its number density (Koga et al. 2019). During this time a sudden brightening at near-infrared wavelengths was observed at Kurdalagon Patera. Although plumes could not be detected directly in these observations, plumes have been detected here before (e.g., by *New Horizons*, Spencer et al. 2007). de Kleer and de Pater (2016a) therefore suggested that the changes observed in the Jovian system may have been caused by an influx of neutral material from a

plume at Kurdalagon Patera, perhaps through a process related to that modeled by McDoniel et al. (2019). In addition, the process by which dust streams in Jupiter's magnetosphere, which are primarily composed of salt (NaCl, Postberg et al. 2006), are expelled from Io's volcanoes is also unknown (e.g., Krüger et al. 2004).

8.4 Plumes: Characteristics, Deposits, and Models

An excellent review of plumes and their deposits is provided by Geissler and Goldstein (2007). Since then more research has been conducted. For example, Geissler and McMillan (2008) summarized *Galileo* observations of Io's plumes, Jessup and Spencer (2012) analyzed *HST*/WFPC2 data of the plumes above Pele, Tvashtar, and Pillan as observed between 1995 and 2007, de Pater et al. (2020b) observed plumes with ALMA during an eclipse, and there have been several developments in the modeling of volcanic plumes. In the next subsection we discuss observations of plumes and their deposits, followed by sections on the thermodynamic properties and on hydrodynamic models of plumes.

8.4.1 Observations of Plumes and Their Deposits

Plumes are easiest to see in sunlight through light scattered off dust particles and condensates in the plume; the plumes typically have a bluish color (e.g., Fig. 8.12a) indicative of light scattered off small ($\lesssim$sub-μm-sized) particles. The plume material coats the surface, resulting in a colorful display, including bright red rings surrounding the vent for Pele-type plumes (Fig. 8.14). The variety of colors is attributed to SO_2-frost, a variety of sulfur allotropes (S_2–S_{20}), and metastable polymorphs of elemental sulfur mixed in other species (Moses and Nash 1991; Carlson et al. 2007). The colors and coverage change on time scales of months–years due to burial by new eruptions, thermal metamorphism (such as annealing of fine-grained frost into coarse-grained ice at the equator), and slow chemical alterations on the surface, such as the change from red short-chain sulfur allotropes to the more stable yellow S_8 which cause a fading of the red rings around plumes once the volcano is no longer active (e.g., Geissler et al. 2004b).

Historically, plumes have been divided into two classes: "Pele-type" plumes reach altitudes over ~400 km and are surrounded by red rings of deposits; in contrast, "Prometheus-type" plumes do not extend much higher in altitude than ~100 km. A plume's radial extent is typically two times larger than its altitude. In Sect. 8.4.2 we expand more on plume classes.

HST observations of large plumes (Pele, Tvashtar, Pillan) show a higher reflectivity (I/F) at 0.33 μm than at 0.26 and 0.41 μm. Based upon Mie calculations, Jessup and Spencer (2012) suggest particle radii of order 0.05–0.1 μm for the particulates in these plumes. Geissler and McMillan (2008) suggested somewhat larger particle

radii ($\sim$0.1 μm) for dust in Prometheus-type plumes, as derived from the linear decrease in I/F between 0.4 and 0.76 μm seen in *Galileo* data. These particles are referred to as "coarse-grained ash" and make up the central columns of Prometheus-type plumes; this ash is entrained in the gas flow when it leaves the surface. The dust mass is typically of order 10^6 to a few $\times 10^7$ kg, or $\sim$1–10% of the gas (SO_2) mass, with the low end for Pele-type, and high end for Prometheus-type plumes (Geissler and McMillan 2008; Jessup and Spencer 2012). This implies a dust production rate of order 10^3–10^4 kg/s assuming a dynamical (in-flight) lifetime of $\sim 10^3$ s. Some (and perhaps all) Prometheus-type plumes have a halo of much smaller-sized (radii $\lesssim$10 nm) particles, with a mass similar or larger than the mass in the gas ($\gtrsim 10^8$ kg); these may be sulfurous snowflakes or droplets condensed from the gas during flight, while the gas is cooling through adiabatic expansion and radiation (Geissler and McMillan 2008).

When observed during an eclipse or at night a plume glows due to bluish gas emissions, likely dominated by SO_2 emissions as seen in the aurora discussed in Sect. 8.3.3. Gas in Prometheus-type plumes reaches altitudes up to $\sim$200–400 km above the surface, i.e., 2–4 times higher than the dust in these plumes, although the halo of tiny snowflakes or droplets covers a similar extent in altitude and radius as the gas (Geissler and McMillan 2008). In Pele-type plumes the dust and gas reach similar ($\sim$400 km) altitudes, indicative of the somewhat smaller sized dust grains mentioned above. The smaller-sized particles and $\gtrsim$10 times less dust mass explains why these Pele-type plumes are more difficult to detect.

Eruptions may last for decades, such as for Pele and Prometheus, which were active during both the *Voyager* and *Galileo* era's. Tvashtar has been erupting intermittently on decade-timescales, being active for months once erupting; a plume and red ring were seen during the *Galileo/Cassini* era (Fig. 8.14). A "re-awakening" was observed in April 2006 with the Keck telescope through a brightening at 1.5–2.4 μm, indicative of a hot spot with a temperature at $\sim$1240 K (Laver et al. 2007); about 10 months later (February/March 2007) a plume and red ring were detected by the *New Horizons* spacecraft (Spencer et al. 2007).

Although large outburst-style eruptions on timescales of hours–days have been reported from data at near-infrared wavelengths, which are sensitive to the temperature of the lava (e.g., Chap. 6), not much is known about potentially short-lived plumes. The presence of plume activity missed by spacecraft has occasionally been inferred through observations of new deposits (see, e.g., the review by Geissler and Goldstein 2007), but this does not provide information on the duration of such plumes. However, although plumes may be active over periods of months, *New Horizons* provided a 5-frame "movie" of Tvashtar's plume showing unsteady dynamics in the particulate canopy with large fluctuations on time scales of minutes suggesting dynamics of the source processes on similar time scales.

The gaseous content of the plumes has been measured from imaging and/or spectroscopy on a few occasions, but the quantitative interpretation of imaging data is complicated by the competing effects of gas and dust, or of different gases, in producing the opacity. Observations include the direct detection of SO_2, S_2, S, and SO over Pele's plume (McGrath et al. 2000; Spencer et al. 2000; Jessup et al. 2007),

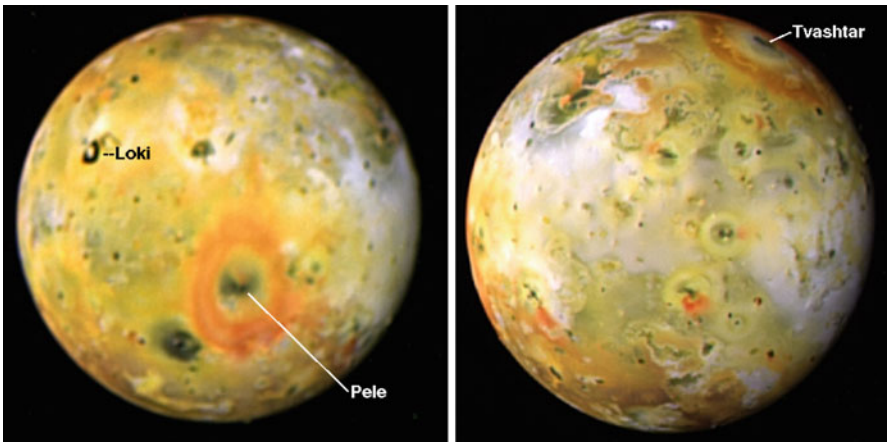

Fig. 8.14 *Galileo* images showing the abundance of colors on Io. The volcanic sites of Loki Patera, Tvashtar Patera and Pele are indicated. The latter two are surrounded by rings of red material, deposits from gigantic plumes that were imaged simultaneously by the *Galileo* and *Cassini* spacecraft. The images were taken in late December 2000 and early January 2001 (PIA02588; NASA/JPL/University of Arizona)

SO_2 at Loki and Pillan (Pearl et al. 1979; Jessup et al. 2007), and more indirect (imaging) evidence of SO_2 and S_2 in Tvashtar's plume (Jessup and Spencer 2012). Although McGrath et al. (2000) reported a SO_2 column density (3.25×10^{16} cm^{-2}) over a region encompassing Pele to be several times larger than in two other regions, this is not direct evidence for volcanically-emitted gas, but may simply reflect variations with longitude and latitude in the overall distribution of SO_2 gas. Roth et al. (2011) modeled the (auroral) emission from Tvashtar's plume while Io was in eclipse to derive a column density in the plume of $\sim 5 \times 10^{15}$ cm^{-2}.

Gaseous plumes can also be discerned in the ALMA spectral maps discussed previously, both in sunlight and in eclipse, taking advantage of the spectral resolution. Figure 8.15 (de Pater et al. 2020b) shows a series of ALMA images at different velocities for the in-sunlight SO_2 data. This series of images reveals that volcanic plumes (in this case above the P207 patera) dominate the emission at large velocities from the line center, ~ -0.8 km/s in frame 1 and $\sim +0.4$ km/s in frame 3, implying that volcanic plumes shape the high-velocity wings of the disk-integrated line profile (fourth frame). Since the high-density "core" or "stem" of the plume only covers a small area compared to the beamsize of the telescope, we most likely see the front-side of the large umbrella-shaped plume in frame 1, and the far-side of the canopy moving away from us in frame 3. These high speeds match the expected gas velocities associated with large plumes when simulating its shape using ballistic trajectories. Occasionally, an entire disk-integrated line profile had been observed to be red-shifted by several tens m/s (Lellouch 1996; de Pater et al. 2020b), attributed to the downward flow of an umbrella-shaped canopy of a plume on the disk.

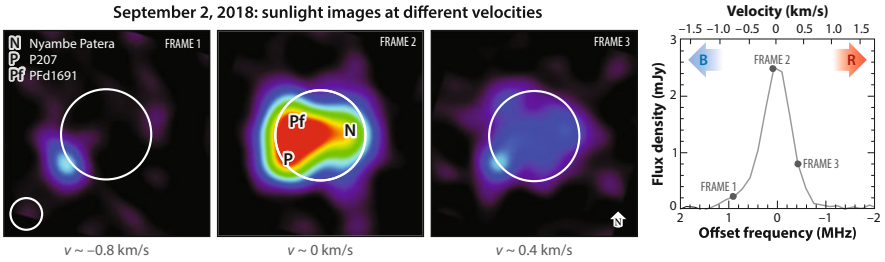

Fig. 8.15 Individual frames at different offset frequencies (velocities) obtained with ALMA on 2 September 2018, when Io was mapped while in-sunlight. Data at two transitions (346.652 and 346.524 GHz) were combined to increase the signal-to-noise. Each frame is averaged over 0.142 km/s (~0.16 MHz), and the line is centered on Io's frame of reference. As in Fig. 8.9, the large circle shows the limb of Io, and the small circle the resolution of the data. The fourth panel shows the disk-integrated line profile, and the grey dots indicate the offset frequency (velocity) of each image in frame 1–3. The symbols B (blueshift) and R (redshift) show the velocities of gas moving towards (B) or away from us (R). The approximate positions of several volcanoes are indicated on frame 2 (de Pater et al. 2020b). Figure reproduced from de Pater et al. (2021)

Eclipse response in the line profiles of regions associated with plumes in ALMA data (Fig. 8.16) show a similar behaviour as the eclipse response of disk-integrated line profiles. In eclipse, the atmospheric columns and temperatures obtained from best fit isothermal hydrostatic models to the spectra remain roughly constant, but the fractional coverage of the atmosphere in the beam decreases. Note that even in plume regions, the fractional coverage of the atmosphere is not unity in sunlight, suggesting that the plume emitting region is not resolved in the observations. The emission shoulders related to plume emissions are clearly visible in the associated spectra. It is clear from the line profiles of the plumes, but also for the disk-integrated profiles in-eclipse, that simple hydrostatic models are not sufficient (de Pater et al. 2020b).

Io's active volcanism must lead to a constant resurfacing of its crust, whether caused by plume deposits, or lava pouring out of vents. A lack of impact craters on Io's surface suggests an upper limit of 10^6–10^7 years on Io's surface age, which implies a global resurfacing rate of 0.1–1 cm/yr (e.g., Carr 1986). Based upon the above mentioned dust production rates in plumes, Geissler and McMillan (2008) conclude that the high resurfacing rate based on the obliteration of all impact craters is likely caused by the emplacement of lava flows rather than deposition of dust from plumes, unless many plumes were missed in *Galileo* observations, or that other material in addition to dust fall-out might be important, such as SO_2 snowfall or direct condensation from the gas phase onto the surface.

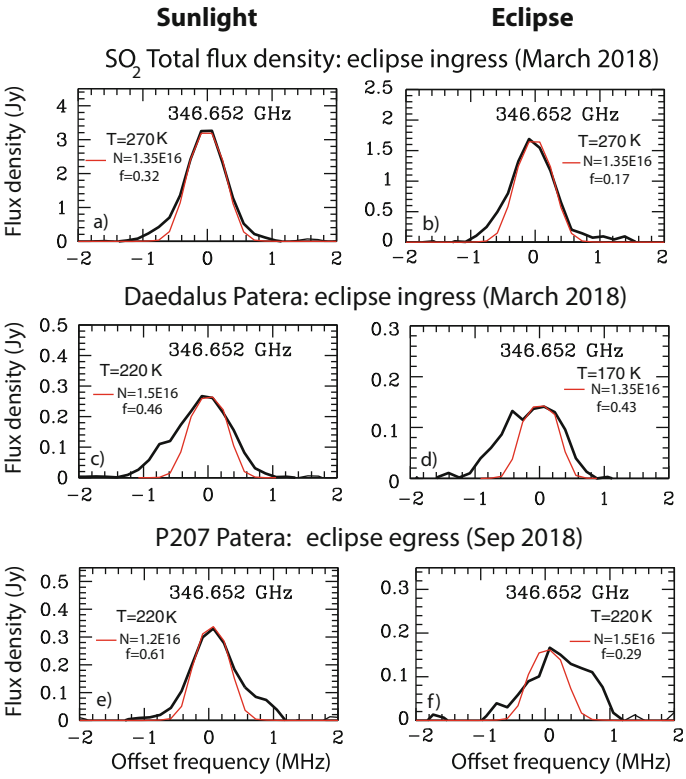

Fig. 8.16 SO_2 line profiles (in black) with superposed the best-fit hydrostatic models (in red). The column density N, temperature T, and fractional coverage f used for fitting are indicated. Both data and models are at a frequency of 346.652 GHz. (**a**) Disk-integrated flux density for Io in sunlight. (**b**) Disk-integrated flux density for Io in eclipse, after eclipse-ingress. (**c**) In-sunlight data for Daedalus Patera, integrated over 1 beam diameter. (**d**) In-eclipse data for Daedalus Patera, integrated over 1 beam diameter, after eclipse-ingress. (**e**) In-sunlight data for P207, integrated over 1 beam diameter. (**d**) In-eclipse data for P207, integrated over 1 beam diameter, before eclipse-egress (Adapted from de Pater et al. 2020b)

8.4.2 Thermodynamic Properties of Plume Classes

Kieffer (1982) investigated potential reservoirs and thermodynamic properties of Io's diverse volcanic plumes. She composed a temperature–entropy diagram, and suggested 5 potential entropy ranges or reservoirs for Io's plumes, varying from low-entropy (reservoir I) to extremely high entropy (reservoir V) eruptions. In connecting these models with observations of plumes, one can distinguish three types of plumes. The majority of plumes fall in the category of the dust-rich Prometheus-type plumes. These appear to "wander" in location (the Prometheus plume migrated over 80 km over a 20-year time interval, Kieffer 2000), and may

originate when hot silicate lava flows advance through a SO_2 snow field. These plumes are referred to as "low-to-moderate entropy" eruptions.

The highly energetic $\gtrsim$400 km high Pele-type plumes are rich in sulfur gases (S_2 and S are both detected above Pele; McGrath et al. 2000; Spencer et al. 2000; Jessup et al. 2007), and contain much less particulate matter (dust and condensates) (Sect. 8.4.1); they therefore are likely higher-entropy eruptions.

A third type are the "stealth" plumes, extremely high-entropy eruptions (Kieffer's reservoir V), from a reservoir of superheated SO_2 vapor in contact with silicate melts about 1.5 km below the surface at pressures of ~40 bar and temperatures of ~1400 K. Since such plumes would consist of essentially pure gas, i.e., without dust or condensates, they cannot be detected in reflected sunlight, and hence were usually not seen by spacecraft. Johnson et al. (1995) suggested that this type of plume might be widespread on Io, such as the plumes and diffuse glows that were imaged over Acala Fluctus by the *Galileo* spacecraft when Io was in eclipse (McEwen et al. 1998), and the diffuse glows and point-like sources the *New Horizons* mission captured during an eclipse, as shown in Fig. 8.12 (Spencer et al. 2007). Johnson et al. (1995) also proposed that these stealth plumes were responsible for the millimeter SO_2 emission, for which an interpretation (Lellouch 1996; Moullet et al. 2008) called for a large number of un-seen plumes in comparison to the visible ones. More evidence for wide-spread stealth volcanism was provided by observations of SO emissions, as discussed in Sect. 8.3.2.2 (de Pater et al. 2020a). This phenomenon could, perhaps, prevent a total collapse of Io's atmosphere during eclipse (de Pater et al. 2020b).

8.4.3 Models of Plumes

In order to learn more about the underlying sources of volcanic explosions, we need to model the plumes and hot spots, the two resulting phenomena that can be observed from afar. In this section we discuss models of plumes. The large umbrella-shaped plumes seen from afar (Fig. 8.17a,b) arise from a vastly smaller, geometrically complex source region through a sequence of non-LTE processes. The overall plume size reflects the source energy (see previous section) in that the thermal energy at the source, which depends on the SO_2 stagnation temperature, T_{stag}, is converted to directed kinetic energy (velocity) during the gasdynamic expansion into the near-vacuum just above the surface. The gas subsequently rises and falls, exchanging directed kinetic energy for potential energy and returning again to kinetic energy before it strikes the surface or shocks and expands further. The peak velocity/altitude is determined by T_{stag} and by whether the gas mass flow rate is sufficient for the gas to be collisional; if it is dense enough to be collisional at high altitudes, the falling gas encounters rising gas and an umbrella-shaped canopy shock wave forms at a height determined by conservation of mass, momentum and energy (App. B in McDoniel 2015), keeping a lid on the canopy size. Such a shock-bound canopy is thus about a factor of two lower in altitude than a simple ballistic

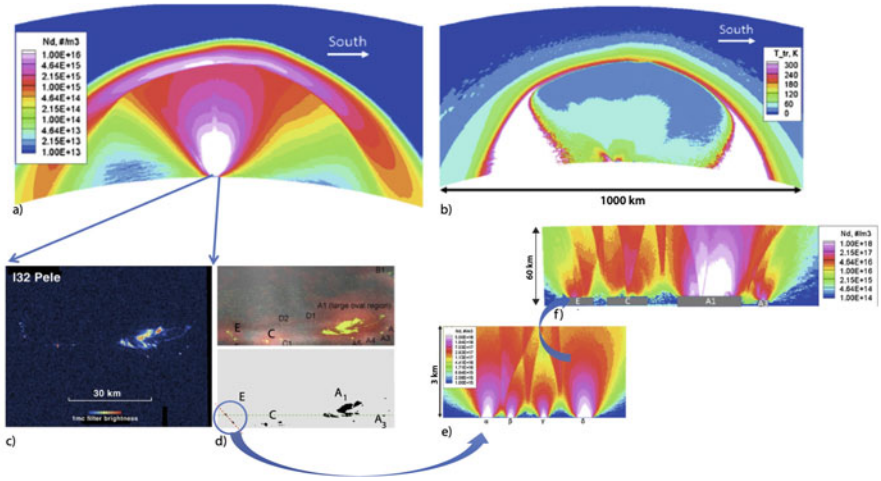

Fig. 8.17 Composite figure from McDoniel et al. (2015) illustrating the development of the Pele plume from multiple source regions into the grand dome canopy seen from a distance. At the top are (**a**) density and (**b**) temperature fields in the umbrella-shaped plume over Io's limb. (**c**) Galileo SSI image of the Pele caldera and (**d**) archipelago of simulated sources. Many little gas/particle jets merge through a sequence of oblique shock and rarefaction waves which, at a set of ever increasing scales, produce a variety of strong density and temperature gradients which appear differently depending on the view direction and cutting plane. (**e**) The circled four tiny sources $\alpha, \beta, \gamma, \delta$ that make up region E in panel (**d**) lead to four interacting jets. A sideways view of the lower 3 km of the plumes is shown along the red dashed line in panel (**d**). These plumes interact with more distant jets higher up, shown in panel (**f**). (**f**) A sideways view of the plumes seen along the green dashed line in panel (**d**), up to an altitude of 60 km. Even at 60 km the region constitutes only a small portion of the "stem" of the grand Pele plume draped over the limb of Io

calculation would indicate. The canopy width depends on whether the gas shocks and also on the initial jet spreading angle near the surface which is determined by geometric details of the vent (McDoniel 2015; Hornung 2016).

Simulations conducted since the review by Geissler and Goldstein (2007) have incorporated most of the physics that was missing before. These simulations include fully three dimensional simulations (McDoniel et al. 2015; Ackley et al. 2021), unsteady plumes interacting with a changing sublimation atmosphere (McDoniel et al. 2017) or undergoing 3D dynamic pulses (Hoey et al. 2021), and plumes at different locations on Io interacting with impinging streams of Jovian plasma and sunlight (Blöcker et al. 2018; McDoniel et al. 2019).

In Fig. 8.17 the large umbrella-shaped plume is sourced from a large number of compact vents. McDoniel et al. (2015) examined how the geometrically complex near-surface sources of Pele's plume of gas and particles merge together through a sequence of oblique gas-dynamic shock and rarefaction waves which turn the direction of the rising and falling gas and particulate streams away from the midline. Sheets of concentrated gas and particles are evident in simulations at low altitudes due to multiple jet-jet interactions, but at higher altitudes they combine into the

broad umbrella shaped canopy as observed by *Voyager, Galileo* and *New Horizons*. At Pele, those detailed near-surface jet-jet interactions leave their imprint on the visible canopy structure, the shape of the reddish deposition ring and the darker silicate deposits which fall inside of the main ring. While the smallest particles track the gas well ($\lesssim$10 nm radii; Sect. 8.4.1), larger micron-scale particles do not and tend to fall shy of the red deposition rings. Similarly, the same modeling approach can be used to infer the overall shape and orientation of the Tvashtar source region from the shape of the surrounding primary red deposition ring (Hoey et al. 2021; Ackley et al. 2021). Sunlight scattered off particulates (dust, condensates, droplets) is typically seen in images (Sect. 8.4.1). The volatile condensates may change size or sublimate during their traverse through the plume, depending on the details of the local gas dynamics. Those phase changes are not obvious, however, in that they depend on, e.g., local gas temperatures, densities, radiation fields, and the particulate motion with respect to the gas. Those interactions are generally not occurring in regions of local thermodynamic equilibrium. For example, the gas kinetic temperature and internal grain/droplet temperature are not likely to be the same at a given point in the plume. Similarly for the gas velocity and particulate velocity. This disequilibrium occurs because the gas density is not large enough outside of the central plume core to sustain enough molecule-particulate collisions for equilibrium to occur.

At lower altitudes within plumes, radiative exchange is important to subsequent plume evolution. The hot SO_2 gas leaving the surface is at a sufficiently high density that it is opaque to radiative emission from the ν_1, ν_2 and ν_3 bands. That is, most of the volume of hot rising gas cannot cool by spontaneous emission from those bands because the respective photon mean free path for re-absorption is insufficient for it to escape the plume core. The gas thus initially expands and cools adiabatically. As the expansion proceeds, however, the gas density and temperature drop and once the density drops enough, the plume core becomes successively more transparent to cooling from the three vibrational bands. For Tvashtar or Pele, the resulting emission surfaces occur around 20–30 km above the surface (Zhang et al. 2003; Hoey et al. 2021). This energy loss ultimately diminishes the ability of the plume to rise to the same height as it would if the flow were everywhere adiabatic. The radiation process depends on the details of the total mass flux, the sizes and shapes of the volcanic sources, the collision cross sections for translation/rotation/vibration energy exchange, the Einstein A coefficients for spontaneous emission, and the photon absorption cross sections.

This dependence of plume gas dynamics on radiative loss is related to what is ultimately observed of the plume from afar. By observing the Doppler shifts of SO_2 lines, one can determine localized flow velocities along the observational line of sight. Moullet et al. (2008) used this method to infer planetary-scale winds (which turned out to mimick a prograde zonal flow), and de Pater et al. (2020b) to determine gas velocities of/in (averaged over the plume area) plumes (e.g., Figs. 8.15 and 8.16). However, as illustrated in Fig. 8.2, because of the huge variations in gas density associated with temperature and velocity changes in the plumes, extremely high spatial resolutions are required to observationally separate velocities in a plume. For comparison, the collisional portion of the sublimation atmosphere only spans

a few scale heights at most and gas temperatures vary by factors of 2-to-5, while the sublimation atmosphere along lines of sight remains nearly transparent to most radiation. Therefore, when looking remotely at a Pele-class plume that is not well resolved spatially, it is not obvious what is observed: hot gas at 1500 K above the vent is expected to expand from a few hundred meters per second to over 1 km/s while its density drops by orders of magnitude. It is not clear whether the gas has reached nearly its ultimate speed ($\sim \sqrt{2 * Cp * T_{stag}}$ for adiabatic flow) before its density drops enough for it to become transparent or whether it becomes transparent much higher up. That is, it is not clear to what depth into the plume core one probes when observing remotely. Similarly, when examining the plume canopy in vibrational/rotational lines it is not clear how those are related to gas velocity or translational (kinetic) temperatures since molecular collision rates are quite low and spontaneous emission losses are important. Thus, interpreting existing observations remains tricky. But simulations remain tricky as well, not so much due to the shortcomings of included physical models, but due to the uncertainty in the many necessary physical boundary conditions, specifically the real "gas-surface interaction" in the broadest sense. While the launch-to-landing gas dynamics can be simulated including the full non-equilibrium physics, the reality of those simulations remains in doubt due to the uncertainties in the many boundary conditions—i.e., mostly the details of the plume source region.

8.5 What Drives Io's Atmosphere?

In the following subsections we address the historic question of the primary "driver" of Io's atmosphere (sublimation, volcanism, sputtering). This question can in fact be interpreted in different ways: (1) what is the "immediate source" of the atmosphere? Or (2) what drives Io's atmospheric dynamics? After reviewing the three possible sources, we will return to this question in Sect. 8.6.

8.5.1 Sublimation-Supported Atmosphere

The fundamental aspect of a sublimation-driven atmosphere that is amenable to observational characterization is that it reacts to changes in insolation on timescales from minutes (eclipse ingress/egress) to hours/days (Io day = 42 h) and years (Io's year = 11.9 years). Io's low surface pressure, typically a few nanobars at most, means that latent heat exchanges are inefficient at redistributing energy, so that individual areas of SO_2 frost assume largely independent, solar-insolation driven, temperatures (Ingersoll et al. 1985; Ingersoll 1989). In a sublimation-driven atmosphere we therefore expect collisionally thick conditions on the day-side in low-latitude regions collapsing to a thin atmosphere on the nightside, in eclipse and at high latitudes.

To determine if the primary immediate source of Io's atmosphere is sublimation, the response of Io's atmosphere to time scales on minutes–hours–years is even more diagnostic than the use of atmospheric bulk properties or spatial distribution, although these bring useful additional constraints. Considerable progress has been achieved in this area since the 2007 Io book, thanks to a large body of thermal-infrared 19-μm observations (Spencer et al. 2005; Tsang et al. 2012; Tsang et al. 2013a,b), as well as 19-μm and sub-millimeter observations of Io going into and coming out of eclipse (Tsang et al. 2016; de Pater et al. 2020b). The latter data were summarized in Sect. 8.3.2.

From a broad coverage of the 19-μm SO_2 observations along Io's orbit around Jupiter, Spencer et al. (2005) determined factor-of-10 larger SO_2 columns on the anti-Jovian hemisphere (180°W) compared to 300°W, in general agreement with the Ly-α maps shown in Fig. 8.6 (Feaga et al. 2009; Giono and Roth 2021). Extending the coverage over a full ionian year, from 2001 to 2013, Tsang et al. (2012, 2013b) established that the SO_2 columns on the anti-Jovian atmosphere peaked at the time of the March 2011 perihelion at 4.955 AU, and reached a 3 times smaller minimum at the March 2005 aphelion (5.459 AU), yielding direct evidence for a largely sublimation-driven atmosphere on the anti-Jovian hemisphere (Fig. 8.18). These annual variations of the SO_2 columns were fit by a combination of a volcanic component (6.5×10^{16} cm^{-2}, making up most of the aphelion atmosphere) and a sublimation component calculated for a frost albedo $A = 0.535$ and thermal inertia $\Gamma = 350$ MKS.

Observational results regarding the diurnal variability of the SO_2 atmosphere are not as definite. "Instantaneous" maps of the SO_2 columns do feature spatial

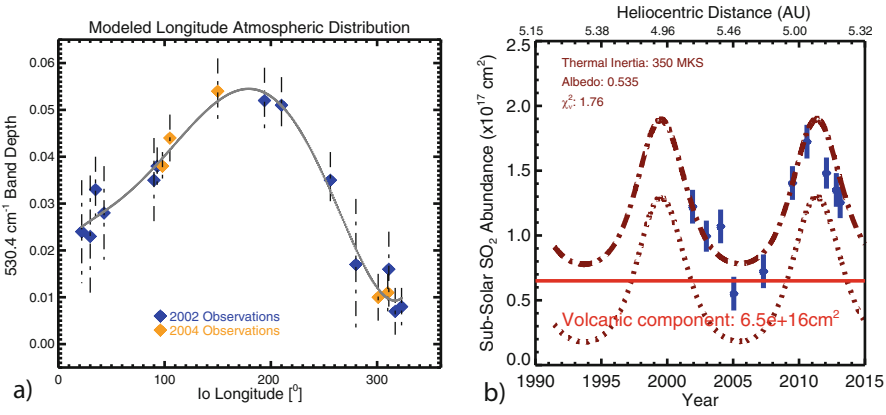

Fig. 8.18 (**a**) Disk-averaged band depth at 530.4 cm^{-1} observed in 2002 (blue) and 2004 (yellow) from Spencer et al. (2005), with a 5th order least-squares polynomial (gray). (**b**) A comparison between retrieved SO2 column densities, after scaling to an Io central longitude of 180° (blue) and a modeled atmosphere in vapor pressure equilibrium with surface frost (dotted), after adding a constant volcanic component (dot-dash), as a function of solar insolation (from Tsang et al. 2013b)

variability, but whether they are purely geographical or also affected by diurnal variations is ambiguous. For example, the individual Ly-α maps of Feaga et al. (2009) do not reveal any obvious decrease of the SO_2 columns towards the terminator. From their 4-μm data, Lellouch et al. (2015) inferred moderate diurnal variations of the equatorial atmosphere, with factor-of-2 lower densities 2.7 h before and 5.3 h after noon, compared to local noon. The most convincing study is from Jessup and Spencer (2015) who used spatially-resolved *HST*/STIS observations to observe regions at 200–250°W longitudes at 2 distinct times of day, differing by 50° of rotation (3.3 h in local time) of Io, disentangling in this manner geographical and diurnal variations, while carefully avoiding volcanic areas. Negligible variation of the SO_2 column with local time was found, consistent with the dawn-to-dusk presence of the atmosphere as derived from Ly-α images. This, however, should not be taken as an argument against a sublimation-driven atmosphere as it can still be consistent with sublimation support by high thermal inertia frost (Spencer et al. 2005).

On the theoretical side, Moore et al. (2009) and Walker et al. (2012), amongst others, show that the surface temperature of the sub-Jovian hemisphere is colder than that of the anti-Jovian side due to the 2-h-long eclipses every orbit (42.5 h), as demonstrated in Fig. 8.19. Since the SO_2 surface pressure virtually follows the saturated vapor curve, based on this figure one would therefore naturally expect a $\sim 4\times$ higher column of gas above the anti-Jovian hemisphere, assuming a more or less uniform ice coverage. The ice coverage, however, varies across the surface. SO_2 fine-grained frost, as indicated by the strong 4.07 μm band, is generally widespread, but most abundant on the anti-Jovian hemisphere and at mid-latitudes (Douté et al. 2001); thick SO_2 frost, traced by the weak 2.12 μm band, is enhanced at equatorial

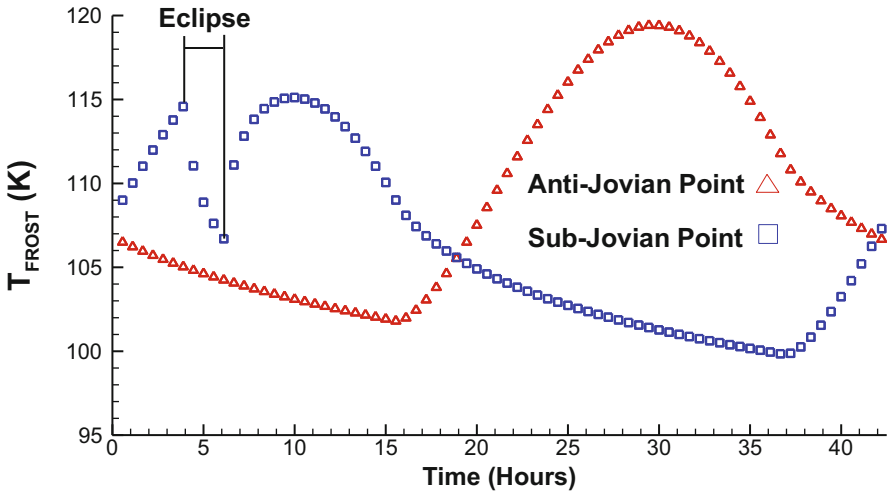

Fig. 8.19 A comparison between the simulated surface frost temperature at the anti-Jovian and sub-Jovian points as a function of time of day (from Walker et al. 2012)

latitudes near 120–180°W (Laver and de Pater 2009; de Pater et al. 2020a). These asymmetries in ice coverage should also contribute to the longitudinal variations in column density. The lower ice coverage on the sub-Jovian hemisphere might be caused by an increased loss due to sputtering during eclipse (Sect. 8.5.3).

The observations of Io's atmosphere in response to eclipse ingress/egress discussed in Sects. 8.3.2 and 8.3.3 provide information on the sublimation aspect of Io's atmosphere on the shortest timescales. As discussed in Sect. 8.3.3, Saur and Strobel (2004) modeled the response of auroral emissions when Io enters an eclipse. They concluded, based on the factor-of-3 decrease in Io's atomic emissions upon eclipse ingress observed by Clarke et al. (1994), that Io's global (background) atmosphere must strongly decrease during eclipse and must therefore be mostly driven by sublimation rather than volcanoes. Similarly, observations of eclipse-ingress both in the mid-IR and sub-mm (ALMA) showed a substantial collapse of the SO_2 atmosphere, and (in the sub-mm) reformation upon egress within about 10 min. A comparison of the ALMA maps with Walker et al. (2012)'s sublimation models (Sect. 8.3.2.1) shows that both collapse and reformation of the atmosphere occur much faster than modeled (∼10 min vs ∼2 h).

Walker et al. (2012)'s model is based upon thermophysical properties of Io's surface (Sect. 8.3.2.1), with horizontal variations in the thermal inertia Γ. Since Γ depends both on composition and compactness (density) of the material, one might expect variations both across the surface (e.g., areas covered by frost and non-frost or rock) and with depth (e.g., deeper layers will be more compacted, and might have a different composition). The thermal inertia for rock and dust is relatively low, while areas covered with SO_2 ice will have a higher Γ. Hence rocky/dusty areas will respond much faster to changes in illumination than areas covered by frost. Hence one expects nearly instantaneous SO_2 condensation on the "bare" rocky/dusty surface when it cools, and sublimation (or desorption) as soon as sunlight hits the rocky surface at dawn. This led to the "Dawn Atmospheric Enhancement" (DAE) in Walker et al. (2012)'s sublimation model (Fig. 8.10 in Sect. 8.3.2.1), with associated standing atmospheric shock waves.

Models that fit the 19-μm eclipse ingress data on minute-time scales shown in Fig. 8.8 (Tsang et al. 2016) require a thermal inertia $\Gamma \simeq 50$ MKS (de Pater et al. 2020b), which is similar to the value of 70 MKS derived by Rathbun et al. (2004) from *Galileo*/PPR data. However, the very small change in the subsurface temperature obtained with ALMA (i.e., ∼1–2 cm below the surface, since one typically probes 10–20 wavelengths deep into the crust) upon eclipse ingress can only be matched with $\Gamma = 320$ MKS (de Pater et al. 2020b), which led the latter authors to suggest a vertical layering of Io's crust: a top ($\lesssim$few mm thick) layer with a low thermal inertia (∼50 MKS) overlying a higher inertia (∼320 MKS) layer. A vertical structure was also proposed by Morrison and Cruikshank (1973) (with Γ's ∼4 times lower) based upon an analysis of eclipse ingress and egress measurements at 20 μm, while Sinton and Kaminsky, (1988), based upon eclipse heating and cooling curves at wavelengths between 3.5 and 30 μm, suggested surface areas with different albedos and Γ's (A = 0.1, $\Gamma = 5.6$ MKS; A = 0.47, $\Gamma = 50$ MKS), with the brighter surface overlying a higher Γ layer.

Based upon the above mentioned discrepancy between observations and sublimation models of eclipse ingress and egress, we suggest that Io's surface is covered everywhere by a low thermal inertia layer, perhaps only a few mm thick, even over areas covered by frost (perhaps due to dust or fluffy plume deposits). We propose that a multi-layer thermophysical model based upon proper surface albedo maps, with a low few-mm thick thermal inertia layer on top (with potentially horizontal variations, but still at a low Γ), overlying higher Γ layers will match the timescales in the data (i.e., a model as, e.g., in de Kleer et al. 2021).

8.5.2 Volcanically-Supported Atmosphere

As discussed in Sect. 8.4.1, numerous volcanic plumes have been detected at seemingly random latitudes. All plumes contain gases, primarily SO_2 as in Io's global atmosphere, with smaller fractions of SO, S, and S_2, depending on plume type. Some volcanoes may expel NaCl and KCl. The dust-to-gas relative content varies from ∼10% in mass for Prometheus-type plumes, to ∼1% in Pele-type plumes, and no dust in stealth volcanoes. The gases in both Prometheus- and Pele-type plumes typically reach altitudes of up to ∼100–400 km, which is well above the exobase (which is at several tens of km; McDoniel et al. 2017). In the following we investigate the effects of volcanic plumes on Io's atmosphere by comparing plume models (Sect. 8.4.3) with data.

McDoniel et al. (2017) examined the plume/atmosphere interaction over a full ionian day for plumes at different latitudes, and showed that one cannot simply add the volcanic and sublimation components to understand an observation. While the total atmospheric mass of SO_2 observable on the (Earth-facing) day side of Io is well controlled by a vapor pressure equilibrium atmosphere over an ice surface in radiative equilibrium with sunshine and in simple hydrostatic equilibrium, the actual material above the surface may be dominated by gas which was just exhausted from a volcano. If a plume is strong enough to launch gas above the nominal exobase, the falling canopy gas mostly settles atop the sublimated component. This raises the surface pressure and drives some of the sublimated gas back into the icy surface until vapor pressure equilibrium at the surface is restored, but leaves a broad layer of volcanic gas atop a sublimated component. If both the sublimated and volcanic components are pure SO_2, the material layers would be distinguishable only based on their temperatures; if the plume material included other gases (e.g., SO, S_n, NaCl, KCl) or nanoparticles, or if the atmospheric component had photodissociation daughter species, the layered components may be chemically distinguishable. These theoretical findings may explain why observed SO_2 column densities above a plume are usually hardly different from their surrounding areas (Lellouch et al. 2015; de Pater et al. 2020b), unless the spatial resolution in the observations would be high enough to distinguish the core of rising gas in a plume.

When the falling canopy of gas from a large plume meets the atmosphere, the plume gas may "bounce" off the atmosphere and thereby heat and increase its

areal extent by a factor of 2–3 (Zhang et al. 2003; McDoniel et al. 2017). This might explain the concentrations of SO_2 emissions near the plumes in ALMA maps (Fig. 8.9).

There can be further modifications on local scales to the plume/sublimation atmosphere as well. As shown by Zhang et al. (2003) in 2D simulations and McDoniel et al. (2017) in 3D simulations, a large Pele-class plume can produce a ring of *reduced* vertical column density above where the main plume deposition ring (i.e., Pele's red ring) is seen. This occurs due to the dynamics of the down-pouring material passing through a curved "re-entry" shock wave (the "bounce"), heating the gas up to levels similar to those seen above the vent. The high pressure will push material away, which results in a depression in the column density at the intersection of the canopy with the sublimation atmosphere, and is also associated with local scouring of surface ice at some times of day.

Finally, there may be a number of active plumes in close proximity to each other (e.g., Fig. 8.17, in which individual jets of Pele are close enough that they interact while still rising) with different strengths, which would complicate the overall interaction between a plume and the sublimation atmosphere. Needless to say that if we consider all these different modeled aspects, together with the variety of viewing angles through a plume (Fig. 8.2) and the spatial resolution of observations, it would be a heroic task to identify parameters in the model to tweak to "match" observations.

8.5.3 Sputtering

Sputtering off a body's surface has been identified as a source of atmosphere for e.g., Mercury and the Moon (where the impinging particles are from the solar wind and micrometeorites), and Giant Planet icy satellites, where the mechanism can coexist with a sublimation source, see e.g. Milillo, et al. (2011) for the Moon and Mercury; Marconi, (2007), Leblanc et al. (2017), Roth et al. (2021) for Ganymede. Sputtering collectively refers to the processes (e.g. direct knocking of atoms from the surface, electronic excitation in the ice) that can lead to the ejection of neutral molecules or atoms into an atmosphere, and is usually accompanied by chemical alteration of the surface (radiolysis).

Sputtering as a source of planetary atmospheres has been reviewed by Cheng and Johnson (1989). Early sputtering models demonstrated that the impact of energetic magnetospheric particles from the Io plasma torus (ions and electrons) can generate an extended, weakly bound, rarefied atmosphere ("corona") around Io. The process is self-limited to column densities of $\sim 10^{15-16}\,\mathrm{cm}^{-2}$ (Lanzerotti et al. 1982) as large gas production halts further penetration of energetic particles, at which point the atmosphere is itself sputtered, with consequences for the upper atmosphere thermal structure (Sect. 8.2.4) and escape (Sect. 8.3.4).

Significant contributions to Io's atmosphere through sputtering can only be expected at times and locations where sublimation and direct volcanic venting are

inefficient in producing an atmosphere. This may occur at high latitudes away from volcanic centers/plumes, or during eclipse or at night. Since surface sputtering also leads to a chemical alteration of the surface, through, e.g., preferential loss of volatile material, sputtering at Io's high latitudes might explain the much darker surface there and the apparent absence of SO_2 ice. Moreover, it may also have led to a preferential loss of volatile ice from Io's sub-Jovian side, since every Io day this side experiences 2-h long eclipses during which time most of the atmosphere is collapsed (Sect. 8.3.2) and hence ions and electrons have more time to impact the sub- versus anti-Jovian hemisphere.

The origin of the sodium and potassium atoms in Io's atmosphere has long been an outstanding puzzle. Although we now know these atoms are derived from NaCl and KCl (Sect. 8.2.3), the question still remains whether the dominant source is sputtering from Io's surface, or volcanically produced. The spatial distribution of NaCl and KCl as mapped with ALMA in 2015 and shown in Fig. 8.20 (Moullet et al. 2015), shows the strongest emission for both species near the volcano Isum Patera (∼206°W longitude, ∼30° latitude). Interestingly, no SO_2 emissions were detected at this location. The alkalis have been mapped with ALMA at several other occasions, and are often localized, do not coincide with SO_2 or SO, and vary drastically over Io's globe (Redwing et al. 2022), yet overall disk-averaged column abundances do not vary much over time (Roth et al. 2020).

The maps in Fig. 8.20 suggest a ratio of ∼5–6 in NaCl/KCl column densities, (Redwing et al. 2022) which is a factor of 2-3 lower than the Na/K ratio in chondrites, but consistent with that measured in Io's extended atmosphere (Brown 2001; Redwing et al. 2022). If sourced volcanically, the difference in the observed

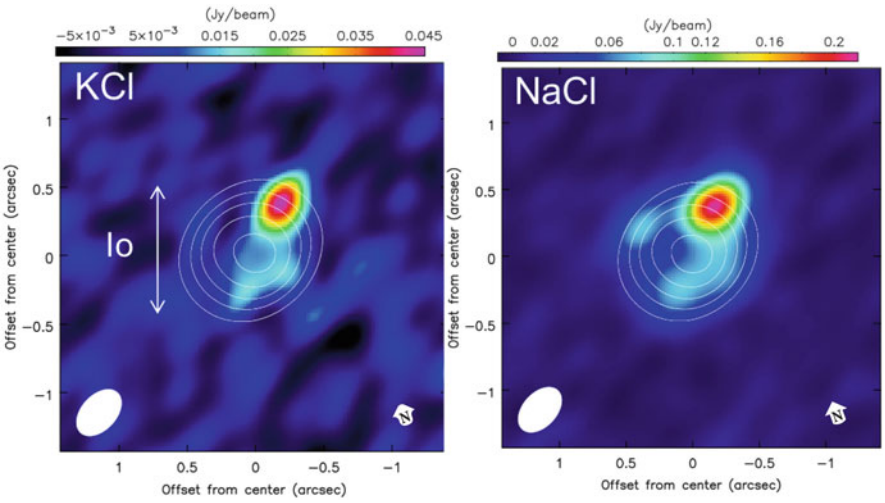

Fig. 8.20 ALMA maps of NaCl and KCl in Io's atmosphere. The data were taken in June 2015, at a spatial resolution of $0.25'' \times 0.4''$. The beam is indicated in the lower left of each figure, and Io's north pole by the arrow in the lower right (Courtesy A. Moullet)

vs chondritic ratio may be caused by the fact that KCl has a lower condensation temperature than NaCl (1173 vs 1363 K), in which case the data may suggest a magma temperature of ∼1300 K (Fegley and Zolotov 2000). Moreover, if indeed volcanically sourced, the magma in the chambers that power volcanoes must have different melt compositions, and/or the magma has access to different surface/subsurface volatile reservoirs, since SO_2 gas is usually not detected at the same locations as NaCl and KCl (de Pater et al. 2020b).

However, once released by volcanoes, NaCl and KCl may also condense/freeze out on Io's surface, in which case plasma impact from the torus could sputter these species back into Io's atmosphere in areas where the atmospheric column density is low ($\lesssim 10^{15-16}$ cm^{-2} Lanzerotti et al. 1982).We note that, regardless of their origin, the short lifetimes require a continuous source to explain the almost-continuous presence (Roth et al. 2020) in Io's atmosphere (Sect. 8.2.3).

8.5.4 Dynamics/winds

Large horizontal variations in SO_2 densities and temperature give rise to horizontal pressure gradients, and hence winds. As suggested by Ingersoll et al. (1985) and Ingersoll (1989), for a sublimation-driven atmosphere this would result in winds away from the subsolar point towards the night side (day-to-night winds) and towards high latitudes. Even if the atmospheric density does not show any clear dusk–dawn variations (Sect. 8.5.1), winds near the terminator might still blow from the day-to-night side, as the atmosphere is still expected to collapse on the nightside due to condensation.

Winds can be observed via their Doppler shift in line profiles, i.e., the entire line can be shifted in frequency, or line profiles can show "shoulders" (e.g., Sect. 8.4.1). Such shifts only provide a line-of-sight component to the wind direction. Interestingly, Moullet et al. (2008) reported strong horizontal winds in the prograde direction from IRAM Plateau de Bure maps, with a beam-integrated limb-to-limb difference of 330 ± 100 m/s. Such winds are hard to reconcile with the above-mentioned models. An enhancement in atmospheric SO_2 near the dawn terminator due to molecules desorbed from a warming rock surface (DAE in Fig. 8.10; Walker et al. 2010) may produce a pressure wind mimicking a prograde zonal wind, although synthetic wind maps based on optical ray tracing through a simulated atmosphere generated by Gratiy et al. (2010) do not closely match those of Moullet et al. (2008). Millimeter-wavelength data at a higher spatial resolution are needed to observe wind profiles in more detail.

It should be understood, however, that winds are not as simple as just some linear combination of day-to-night, volcanic plumes, DAE disturbances, etc. For example, we note in Fig. 8.21 that even though a massive Pele-class plume produces relatively localized column density disturbances (positive in the center, negative in the ring), its influence on the winds may extend over half of the hemisphere visible from Earth.

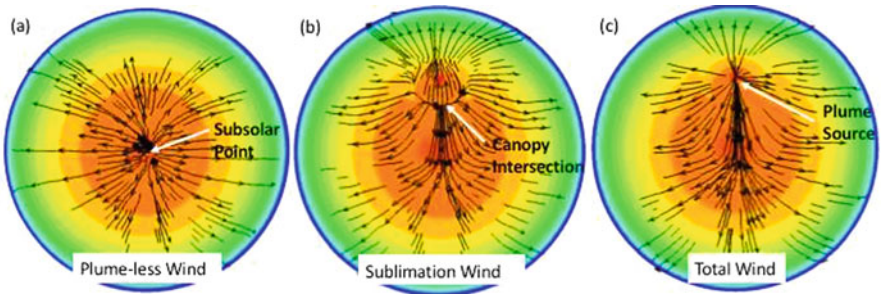

Fig. 8.21 Simulation of a hypothetical Pele-class plume at 30° N on the daylit side of Io. (**a**) Column density color contours and wind vectors in the absence of a plume. (**b**) Color contours show column density with a Pele-class plume included at 30° N but the wind vectors only show the sublimation component of the atmosphere; note how the plume drags or deforms the sublimation component. (**c**) Again, contours represent column density of the composite atmosphere. Now, the wind vectors represent the column-mass-averaged composite value showing broad influence of the plume over northern hemisphere (McDoniel et al. 2017)

Even without the presence of plumes, full planet-scale simulations of an SO_2 and SO atmosphere suggest possibly grossly different wind patterns approaching the terminator and on the night side for the two species. This highlights the fact that a wind only can be represented by a single vector value at each point in space if the gas flow is dense enough to be fully continuum—But Io's plumes and atmosphere are sufficiently rarefied that the wind speed or its direction may not be a unique value.

Figure 8.22 is from Walker's 2012 dissertation, the most physically comprehensive atmosphere simulation to date, notably including photochemistry and plasma-impact chemistry for several species. It also includes plasma pressure due to electric and magnetic fields around Io which can drive winds. The simulated details are remarkable and include a prograde equatorial jet of gas extending much of the way from the day side across the leading hemisphere towards the cold nightside. On the leading side the jets (one prograde, one retrograde) collapse into the solid surface, being viscously dissipated as the atmosphere thins out. Associated with the jet are cyclonic and anticyclonic winds at higher nighttime latitudes. The wind fields are similar for SO_2, S, O, and O_2 where the atmosphere is dense enough to be collisional. These complexities, especially for species other than SO_2, are driven largely by the specifics of the species' chemical source/sink mechanisms and the (residence time) interaction of the species with the solid surface. Perhaps future ALMA observations at high spatial resolution may observe these predicted species' wind and concentration patterns.

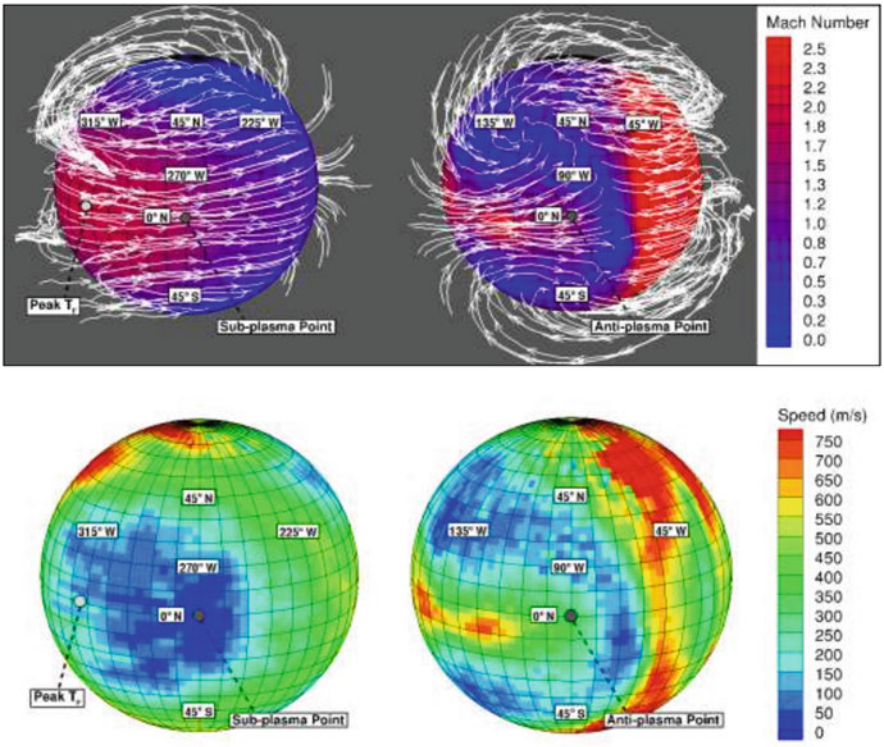

Fig. 8.22 Wind simulations from Walker (2012). In the top two subfigures are wind stream traces overlaid on contours of SO_2 flow Mach number at an altitude of 10 km for the (left) trailing and (right) leading hemispheres. The sub-plasma and anti-plasma points are shown. The subsolar longitude is 342°, a time ∼9° prior to eclipse. Hence, the trailing hemisphere shows mostly the day side, and the leading hemisphere the night side. The lower two subfigures illustrate actual wind speeds at 10 km altitude

8.6 Conclusions and Next Steps

As shown by the data and models presented in this review, we have learned a great deal about Io's atmosphere since the *Galileo* era. However, many questions still remain, and new questions have surfaced, as summarized below.

In Sect. 8.5 we addressed the historic question of the primary "driver" of Io's atmosphere (sublimation, volcanism, sputtering), and distinguished between the immediate source of gas and dynamics in Io's atmosphere. Based upon the large body of data combined with their analyses since the 2007 Io book, it is clear that the immediate source of Io's atmosphere is sublimation/condensation of SO_2. Yet, volcanoes do have a substantial impact on its atmosphere and surface, and may at times and certainly locally be dominant.

While the main source of the observed SO is most likely photodissociation of SO_2, some fraction must be sourced from volcanoes, including stealth volcanism. The main source of Na, K and Cl is photodissociation from NaCl and KCl. Some small fraction of sulfur may also be produced via photochemistry, but the main source of S_2 is volcanic; without it there would not be red deposition rings around Pele-type volcanoes. NaCl and KCl are also most likely volcanic in origin, though some of what we see at higher latitudes, where the column density of SO_2 gas is low enough for ions/electrons from the plasma torus to reach the surface, could have been produced via surface sputtering on salts condensed on the surface. Interestingly, if indeed NaCl and KCl originate from volcanic vents, these do not expel much, if any, SO_2 gas, indicative of variations in magma composition between different volcanoes.

Observations during eclipse ingress and egress show a near-instantaneous decrease in surface temperature ($\sim$2 min) and collapse of a large fraction of the SO_2 atmosphere ($\lesssim$10 min). This is much faster than current models predict. The not-complete atmospheric collapse has been predicted by models, though it is not clear what prevents the SO_2 atmosphere from complete collapse: a layer of non-condensibles as predicted by models, and/or volcanic activity. In addition, although SO itself is not condensible, its significant decrease during eclipse shows that self-reactions on the surface occur at a much faster rate than anticipated.

The near-collapse of Io's SO_2 atmosphere during eclipse and on the night side must trigger winds in the atmosphere: condensation onto the surface must cause a down-pour of gas towards the surface when it is no longer supported from below, while high gas densities during the day and low densities at night and at high latitudes result in winds from high-to-low pressure regions. However, none of the predicted winds have been measured directly. If anything, at millimeter wavelengths a zonal wind has been measured (Moullet et al. 2008), rather than a day-to-night flow.

Volcanic gas plumes are easiest to discern and compare to models at night or during an eclipse; as soon as the SO_2 atmosphere re-forms during the day or after eclipse egress, the falling plume "meets" the atmosphere, and models show a complex interaction, with lateral and vertical variations in density and temperature, as well as the formation of winds. With the relatively low spatial resolution of the present data from Earth it is difficult to compare the models and data in detail, in particular with the realization that plumes are seen under different viewing geometries (e.g., Fig. 8.2), where the line of sight "slices" through different regimes of density and temperature. Perhaps more progress on the observational side (short of sending a spacecraft) can be made by mapping Io at mm-wavelengths at a higher spatial resolution and sensitivity with ALMA using transitions over a broad range of energies. Ideally, observations at high spatial resolution will be obtained during eclipse and ingress/egress at a minute-time resolution.

Yet, it is comforting that models and data agree on some aspects: when the models are convolved down to the same resolution as the data, neither the model nor data show an enhancement in column density above a plume (Lellouch et al. 2015; de Pater et al. 2020b); the models show an enhancement directly over the

vent, which requires a much higher spatial resolution than currently observationally available. Also, the observed brightening and expansion of the SO_2 emissions near volcanic plumes upon eclipse egress agree between models and data, when comparing a modeled plume during an Io-day (McDoniel et al. 2017) with the ALMA data. Note that the "plume bounces" expand the area of volcanic-sourced gas around a plume considerably compared to the case of a nightside plume, which may explain the morphology of ALMA maps in sunlight.

Despite considerable advances in our understanding of Io's atmosphere and plumes, there still are a large number of unsolved problems and questions:

1. What is the impact of Io's volcanic eruptions on its global atmosphere?
2. How do volcanic plumes and sublimated components interact, and how can we best compare the models with data?
3. Io's SO_2 atmosphere does not completely collapse during eclipse; what is the reason?
4. Io's atmosphere collapses during eclipse ingress and reforms upon egress much faster than models predict; how to update models to match the data?
5. How much does surface sputtering contribute to the atmosphere? Are there areas on Io where the atmosphere is collisionally thin, so that ions and electrons from the plasma torus can penetrate down to the surface?
6. What is the origin of NaCl and KCl, and why are they not co-located with SO_2?
7. What is the atmospheric temperature profile (in particular close to the surface), and how does it vary across Io, and how is it affected by volcanic plumes?
8. What are the atmospheric wind patterns? Are there large-scale zonal winds, day-to-night winds, rapid winds away from plumes, and can one discern the effect of the plasma flow?
9. What are the details of atmospheric loss processes (gas and dust), including atmosphere—magnetosphere connections during quiescent periods and volcanic eruptions?

Acknowledgments We like to thank Joachim Saur and Darrell Strobel for helping us understand the variations in auroral and plume emissions upon eclipse ingress, Laurence Trafton for providing Fig. 8.13, and Lorenz Roth for providing a detailed and helpful review of our manuscript. DG acknowledges support in part from NASA award number 80NSSC21K0830

References

Ackley, P., Hoey, W., Trafton, L., Goldstein, D.B., Varghese, P.L.: Hybrid dust-tracking method for modeling Io's Tvashtar volcano plume. Icarus **359**, 114274 (2021)

Ballester, G.E., McGrath, M.A., Strobel, D.F., Zhu, X., Feldman, P.D., Moos, H.W.: Detection of the SO_2 Atmosphere on Io with the Hubble Space Telescope. Icarus, **111**, 2–17 (1994)

Binder, A.P., Cruikshank, D.P.: Evidence for an atmosphere on Io. Icarus **3**, 299–305 (1964)

Blöcker, A., et al.: MHD modeling of the plasma interaction with Io's asymmetric atmosphere. J. Geophys. Res. Space Phys. **123**(11), 9286–9311 (2018)

Brown, R.A.: Optical line emission from Io. In: Woszczyk, A., Iwaniszewska, C. (eds.) Exploration of the Planetary System (IAU Symposium 65), pp. 527–531. Reidel, Dordrecht (1974)
Brown, R.A.: The Jupiter hot plasma torus: Observed electron temperature and energy flows. Astrophys. J. **244**, 1072–1080 (1981)
Brown, M.E.: Potassium in Europa's atmosphere. Icarus **151**, 190–195 (2001)
Cantrall, C., de Kleer, K., de Pater, I., Williams, D.A., Davies, A.G., Nelson, D.: Variability and geologic associations of volcanic activity on Io in 2001–2016. Icarus **312**, 267–294 (2018)
Carlson, R.W., Kargel, J.S., Douté, S., Soderblom, L.A., Dalton, B.: Io's surface composition. In: Lopes, R.M., Spencer, J.R. (eds.) Io after Galileo: A New View of Jupiter's Volcanic Moon, pp. 193–229. Springer. ISBN 3-540-34681-3 (2007)
Carr, M.H.: Silicate volcanism on Io. J. Geophys. Res. **91**, 3521–3532 (1986)
Cheng, A.F., Johnson, R.E.: Effects of magnetospheric interactions on origin and evolution of atmospheres. In: Atreya, S.K., Pollack, J.B., Matthews, M.S. (eds.) Origin and Evolution of Planetary and Satellites Atmospheres, pp. 683–722. University of Arizona Press, Tucson (1989)
Clarke, J.T., Ajello, J., Luhmann, J., Schneider, N., Kanik, I.: Hubble Space Telescope UV spectral observations of Io passing into eclipse. J. Geophys. Res. **99**, 8387–8402 (1994)
de Kleer, K., de Pater, I.: Time variability of Io's volcanic activity from near-IR adaptive optics observations on 100 Nights in 2013–2015. Icarus **280**, 378–404 (2016a)
de Kleer, K., de Pater, I.: Spatial distribution of Io's volcanic activity from near-IR adaptive optics observations on 100 nights in 2013–2015. Icarus **280**, 405–414 (2016b)
de Kleer, K., de Pater, I., Molter, E., Banks, E., Davies, A.G., et al.: Io's volcanic activity from time-domain adaptive optics observations: 2013–2018. Astron. J. **158**, 129 (14 pp.) (2019a).
de Kleer, K., de Pater, I., Ádámkovics, M.: Emission from volcanic SO gas on Io at high spectral resolution. Icarus **317**, 104–120 (2019b)
de Kleer, K., Butler, B., de Pater, I., Gurwell, M., Moullet, A., Trumbo, S., Spencer, J.: Thermal properties of Ganymede's surface from millimeter and infrared emission. PSJ **2**, 5 (2021). https://doi.org/10.3847/PSJ/abcbf4
de Pater, I., Roe, H.G., Graham, J.R., Strobel, D.F., Bernath, P.: Detection of the forbidden SO $a^1\Delta \rightarrow X^3\Sigma^-$ Rovibronic transition on Io at 1.7 μm. Icarus Note **156**, 296–301 (2002)
de Pater, I., Laver, C., Marchis, F., Roe, H.G., Macintosh, B.A.: Spatially resolved observations of the forbidden SO $a^1\Delta \rightarrow X^3\Sigma^-$ Rovibronic transition on Io during an eclipse. Icarus **191**, 172–182 (2007)
de Pater, I., de Kleer, K., Ádámkovics, M.: High spatial and spectral resolution observations of the forbidden 1.707 μm Rovibronic SO emissions on Io: Evidence for widespread stealth volcanism. Planet. Sci. J. **1** (2020a). https://doi.org/10.3847/PSJ/ab9eb1
de Pater, I., Luszcz-Cook, S., Rojo, P., Redwing, E., de Kleer, K., Moullet, A.: ALMA observations of Io going into and coming out of Eclipse. Planet. Sci. J. **1**, 60 (25 pp.) (2020b)
de Pater, I., Keane, J.T., de Kleer, K., Davies, A.G.: A 2020 observational perspective of Io. Annu. Rev. Earth Planet. Sci. **49**, 633–668 (2021). https://doi.org/10.1146/annurev-earth-082420-095244
Dols, V.J., Delamere, P.A., Bagenal, F., Kurth, W.S., Paterson, W.R.: Asymmetry of Io's outer atmosphere: Constraints from five Galileo flybys. J. Geophys. Res. **117**, E10010 (2012). https://doi.org/10.1029/2012JE004076
Douté, S. Schmitt, B., Lopes-Gautier, R., Carlson, R., Soderblom, L., Shirley, J., Galileo NIMS Team: Mapping SO_2 frost on Io by the modeling of NIMS hyperspectral images. Icarus **149**, 107 (2001)
Feaga, L.M., McGrath, M., Feldman, P.D., Strobel, D.F.: Detection of atomic chlorine in Io's atmosphere with the Hubble Space Telescope GHRS. Astrophys. J. **610**, 1191–1198 (2004)
Feaga, L.M., McGrath, M., Feldman, P.D.: Io's dayside SO_2 atmosphere. Icarus **201**, 570–584 (2009)
Fegley, B., Zolotov, M.Yu.: Chemistry of sodium, potassium, and chlorine in volcanic gases on Io. Icarus **148**, 193–210 (2000)

Feldman, P.D., Strobel, D.F., Moos, H.W., Retherford, K.D., Wolven, B.C., McGrath, M.A., Roesler, F.L., Woodward, R.C., Oliversen, R.J., Ballester, G.E.: Lyman-α imaging of the SO_2 distribution on Io. Geophys. Res. Lett. **27**, 1787–1790 (2000)

Geissler, P.E., Goldstein, B.D.: Plumes and their deposits. In: Lopes, R.M., Spencer, J.R. (eds.) Io after Galileo: A New View of Jupiter's Volcanic Moon, pp. 163–192. Springer. ISBN 3-540-34681-3 (2007)

Geissler, P., McMillan, M.T.: Galileo observations of volcanic plumes on Io. Icarus **197**, 505–518 (2008)

Geissler, P.E., McEwen, A.S., Ip, W., Belton, M.J.S., Johnson, T.V., Smyth, W.H., Ingersoll, A.P.: Galileo imaging of atmospheric emissions from Io. Science **285**, 870–874 (1999)

Geissler, P.E., Smyth, W.H., McEwen, A.S., Ip, W., Belton, M.J.S., Johnson, T.V., Ingersoll, A.P., Rages, K., Hubbard, W., Dessler, A.J.: Morphology and time variability of Io's visible aurora. J. Geophys. Res. **106**, 26,137–26,146 (2001)

Geissler, P., McEwen, A., Porco, C., Strobel, D.F., Saur, J., et al.: Cassini observations of Io's visible aurorae. Icarus **172**, 127–140 (2004a)

Geissler, P., McEwen, A.S., Phillips, C.B., Keszthelyi, L.P., Spencer, J.: Surface changes on Io during the Galileo mission. Icarus **169**, 29–64 (2004b)

Giono, G., Roth, L.: Io's SO_2 atmosphere from HST Lyman-α images: 1997 to 2018. Icarus **359**, 114212 (2021)

Gratiy, S.L., Walker, A.C., Levin, D.A., Goldstein, D.B., Varghese, P.L., et al.: Multi-wavelength simulations of atmospheric radiation from Io with a 3-D spherical-shell backward Monte Carlo radiative transfer model. Icarus **207**, 394–408 (2010)

Grava, C., Schneider, N.M., Leblanc, F., Morgenthaler, J.P., Mangano, V., Barbieri, C.: Solar control of sodium escape from Io. J. Geophys. Res. **119**, 404–415 (2014)

Hendrix, A.R., Barth, C.A., Hord, C.W.: Io's patchy SO_2 atmosphere as measured by the Galileo ultraviolet spectrometer. JGR, **104**, 11817–11826 (1999)

Hoey, W., Trafton, L., Ackley, P., Goldstein, D.B., Varghese, P.L.: Variations in the canopy shock structures of massive extraterrestrial plumes: Parametric DSMC simulation of the 2007 Tvashtar observations. Icarus **363**, 114431 (2021)

Hornung, H.G.: A model problem for a supersonic gas jet from a moon. J. Fluid Mech. **795**, 950–971 (2016)

Ingersoll, A.P.: Io meteorology: How atmospheric pressure is controlled locally by volcanos and surface frosts. Icarus **81**, 298–313 (1989)

Ingersoll, A.P., Summers, M.E. Schlipf, S.G.: Supersonic meteorology of Io: Sublimation-driven flow of SO_2. Icarus **64**, 375–390 (1985)

Jessup, K.L., Spencer, J.R.: Characterizing Io's Pele, Tvashtar and Pillan plumes: Lessons learned from Hubble. Icarus **218**, 378–405 (2012)

Jessup, K.L., Spencer, J.R.: Spatially resolved HST/STIS observations of Io's dayside equatorial atmosphere. Icarus **248**, 165–189 (2015)

Jessup, K.L., Spencer, J.R., Yelle, R.: Sulfur volcanism on Io. Icarus **192**, 24–40 (2007)

Johnson, T.V., Matson, D.L., Blaney, D.L., Veeder, G.J., Davies, A.: Stealth plumes on Io. Geophys. Res. Lett. **22**, 3293–3296 (1995)

Kieffer, S.W.: Ionian volcanism. In: Morrison, D. (ed.) Satellites of Jupiter, pp. 647–723. Univ. of Ariz. Press (1982)

Kieffer, S.W., Lopes-Gautier, R., McEwen, A., Smythe, W., Keszthelyi, L., Carlson, R.: Prometheus: Io's wandering plume. Science **288**, 1204–1208 (2000)

Kliore, A., Cain, D.L., Fjeldbo, G., Seidel, B.L., Rasool, S.I.: Preliminary results on the atmospheres of Io and Jupiter from the *Pioneer 10* S-Band occultation experiment. Science **183**, 323–324 (1974)

Koga, R., Tsuchiya, F., Kagitani, M., Sakanoi, T., Yoshioka, K., Yoshikawa, I., et al.: Volcanic change of Io's neutral oxygen cloud and plasma torus observed by Hisaki. J. Geophys. Res. Space Phys. **124**, 10318–10331 (2019)

Kosuge, S., Aoki, K., Inoue, T., Goldstein, D.B., Varghese, P.L.: Unsteady flows in Io's atmosphere caused by condensation and sublimation during and after eclipse: Numerical study based on a model Boltzmann equation. Icarus **221**, 658–669 (2012)
Krüger, H., Horányi, M., Krivov, A.V., Graps, A.L.: Jovian dust: streams, clouds and rings. In: Bagenal, F., Dowling, T.E., McKinnon, W. (eds.) Jupiter: Planet, Satellites & Magnetosphere. Cambridge University Press, Cambridge, UK (2004)
Kupo, I., Mekler, Yu., Eviatar, A.: Detection of ionized sulfur in the Jovian magnetosphere. Astrophys. J. Lett. **205**, L51–L53 (1976)
Lanzerotti, L.J., Brown, W.L., Augustyniak, W.M., Johnson, R.E., Armstrong, T.P.: Laboratory studies of charged particle erosion of SO_2 ice and applications to the frosts of Io. Astrophys. J. **259**, 920–929 (1982)
Laver, C., de Pater, I., Marchis, F.: Tvashtar awakening detected in April 2006 with OSIRIS at the W.M. Keck Observatory. Icarus **191**, 749–754 (2007)
Laver, C., de Pater, I.: The global distribution of Sulfur Dioxide ice on Io, observed with OSIRIS on the W. M. Keck telescope. Icarus **201**, 172–181 (2009)
Leblanc, F., Oza, A.V., Leclercq, L., Schmidt, C., Cassidy, T., Modolo, R., Chaufray, J.Y., Johnson, R.E.: On the orbital variability of Ganymede's atmosphere. Icarus **293**, 185–198 (2017)
Lellouch, E.: Urey Prize Lecture. Io's atmosphere: not yet understood. Icarus **124**, 1–21 (1996)
Lellouch, E., Belton, M.J.S., de Pater, I., Gulkis, S., Encrenaz, T.: Io's atmosphere from microwave detection of SO_2. Nature **346**, 639–641 (1990)
Lellouch, E., Belton, M., de Pater, I., Paubert, G., Gulkis, S., Encrenaz, T.: The structure, stability, and global distribution of Io's atmosphere. Icarus **98**, 271–295 (1992)
Lellouch, E., Strobel, D., Belton, M.J.S., Summers, M.E., Paubert, G., Moreno, R.: Detection of sulfur monoxide in Io's atmosphere. Astrophys. J. Lett. **459**, L107–L110 (1996)
Lellouch, E., Paubert, G., Moses, J.I., Schneider, N.M., Strobel, D.F.: Volcanically-emitted sodium chloride as a source for Io's neutral clouds and plasma torus. Nature **421**, 45–47 (2003)
Lellouch, E., McGrath, M.A., Jessup, K.L.: Io's atmosphere. In: Lopes, R.M., Spencer, J.R. (eds.) Io after Galileo: A New View of Jupiter's Volcanic Moon, pp. 231–264. Springer. ISBN 3-540-34681-3 (2007)
Lellouch, E., Ali-Dib, M., Jessup, K.-L., Smette, A., Käufl, H.-U., Marchis, F.: Detection and characterization of Io's atmosphere from high-resolution 4-μm spectroscopy. Icarus **253**, 99–114 (2015)
Marconi, M.L.: A kinetic model of Ganymede's atmosphere. Icarus **190**, 155–174 (2007)
McDoniel, W.J.: Realistic simulation of Io's Pele Plume and its effect on Io's atmosphere. University of Texas PhD Dissertation (2015)
McDoniel, W.J., Goldstein, D.B., Varghese, P.L., Trafton, L.M.: Three-dimensional simulation of gas and dust in Io's Pele Plume. Icarus **257**, 251–274 (2015)
McDoniel, W.J., Goldstein, D.B., Varghese, P.L., Trafton, L.M.: The interaction of Io's plumes and sublimation atmosphere. Icarus **294**, 81–97 (2017)
McDoniel, W.J., Goldstein, D.B., Varghese, P.L., Trafton, L.M.: Simulation of Io's plumes and Jupiter's plasma torus. Phys. Fluids **31**, 077103 (2019)
McEwen, A.S., Keszthelyi, L., Spencer, J.R., Schubert, G., Matson, D.L., et al.: High-temperature silicate volcanism on Jupiter's Moon Io. Science **281**, 87–90 (1998)
McGrath, M.A., Belton, M.J.S., Spencer, J.R., Sartoretti, P.: Spatially resolved spectroscopy of Io's Pele plume and SO_2 atmosphere. Icarus **146**, 476–493 (2000)
McGrath, M.A., Lellouch, E., Strobel, D.F., Feldman, P.D., Johnson, R.E.: Satellite atmospheres. In: Bagenal, F., Dowling, T.E., McKinnon, W. (eds.) Jupiter: Planet, Satellites & Magnetosphere, pp. 457–483. Cambridge University Press, Cambridge, UK (2004)
Mendillo, M., Baumgardner, J., Flynn, B., Hughes, J.W.: The extended sodium nebula of Jupiter. Nature **348**, 31–314 (1990)
Mendillo, M., Wilson, J., Spencer, J., Stansberry, J.: Io's volcanic control of Jupiter's extended neutral clouds. Icarus **170**, 430–442 (2004)
Milillo, A., Orsini, S., Hsieh, K.C., Baragiola, R., Fama, M., Johnson, R., Mura, A., Plainaki, C., Sarantos, M., Cassidy, T.A., De Angelis, E., Desay, M., Goldstein, R., Ip, W.-H., Killem, R.,

Livi, S.: Observing planets and small bodies in sputtered high-energyatom fluxes. JGR **116**, AO7229 (2011)
Moore, C., Goldstein, D.B., Varghese, P., Trafton, L., Stewart, B.: 1-D DSMC simulation of Io's atmospheric collapse in eclipse. Icarus **201**, 585–597 (2009)
Morabito, L.A., Synnott, D.P., Kupferman, P.N., et al.: Discovery of currently active extraterrestrial volcanism. Science **204**, 972 (1979)
Morrison, D., Cruikshank, D.P.: Thermal properties of the Galilean satellites. Icarus **18**, 224–236 (1973)
Moses, J.I., Nash, D.B.: Phase transformations and the spectral reflectance of solid sulfur - Can metastable sulfur allotropes exist on Io? Icarus **89**, 277–304 (1991)
Moses, J.I., Zolotov, M.Y., Fegley, B.: Photochemistry of a volcanically driven atmosphere on Io: Sulfur and oxygen species from a Pele-type eruption. Icarus **156**, 76–106 (2002a)
Moses, J.I., Zolotov, M.Y., Fegley, B.: Alkali and chlorine photochemistry in a volcanically driven atmosphere on Io. Icarus **156**, 107–135 (2002b)
Moullet, A., Lellouch, E., Moreno, R., Gurwell, MA., Moore, C.: First disk- resolved millimeter observations of Io's surface and SO_2 atmosphere. Astrophys. Astron. **482**, 279–292 (2008)
Moullet, A., Gurwell, M.A., Lellouch, E., Moreno, R.: Simultaneous mapping of SO_2, SO, NaCl in Io's atmosphere with the submillimeter array. Icarus **208**, 353–365 (2010)
Moullet, A., Lellouch, E., Moreno, R., Gurwell, M., Black, J.H., Butler, B.: Exploring Io's atmospheric composition with APEX: First measurement of $^{34}SO_2$ and tentative detection of KCl. Astrophys. J. **776**, 32, 9 pp. (2013). https://doi.org/10.1088/0004-637X/776/1/32
Moullet, A., Lellouch, E., Gurwell, M., Moreno, R., Black, J., Butler, B.: Distribution of alkali gases in Io's atmosphere. In: AAS DPS Meeting #47, Abstract 311.31 (2015)
Peale, S.J., Cassen, P., Reymolds, R.T.: Melting of Io by tidal dissipation. Science **203**, 892–894 (1979)
Pearl, J.C., Hanel, R., Kunde, V., Maguire, W., Fox, K., et al.: Identification of gaseous SO_2 and new upper limits for other gases on Io. Nature **288**, 757–758 (1979)
Postberg, F., Kempf, S., Srama, R., Green, S.F., Hillier, J.K., McBride, N., Grün, E.: Composition of jovian dust stream particles. Icarus **183**, 12–134 (2006)
Rathbun, J.A., Spencer, J.R., Tamppari, L.K., Martin, T.Z., Barnard, L., Travis, L.D.: Mapping of Io's thermal radiation by the Galileo photopolarimeter-radiometer (PPR) instrument. Icarus **169**, 127–139 (2004)
Redwing, E., de Pater, I., Luszcz-Cook, S., de Kleer, K., Moullet, A., Rojo, P.: NaCl and KCl in Io's atmosphere. Planet. Sci. J., **3**:238, 11 (2022)
Retherford, K.D.: Io's aurora: HST/STIS observations. PhD thesis, Johns Hopkins University, Baltimore, MD (2002)
Retherford, K.D., Spencer, J.R., Stern, S.A., Saur, J., Strobel, D.F., et al.: Io's atmospheric response to eclipse: UV aurorae observations. Science **318**, 237–240 (2007)
Retherford, K.D., Roth, L., Becker, T.M., Feaga, L.M., Tsang, C.C.C., Jessup, K.L., Grava, C.: Io's atmosphere silhouetted by Jupiter Ly-α. Astron. J. **158**, 154 (2019)
Roesler, F.L., Moos, H.W., Oliversen, R.J., Woodward, Jr, R.C., Retherford, K.D., Scherb, F., McGrath, M.A., Smyth, W.H., Feldman, P.D., Strobel, D.F.: Far-ultraviolet imaging spectroscopy of Io's atmosphere with HST/STIS. Science **283**, 353–356 (1999)
Roth, L., Saur, J., Retherford, K.D., Strobel, D.F., Spencer, J.R.: Simulation of Io's auroral emission: Constraints on the atmosphere in eclipse. Icarus **214**, 495–509 (2011)
Roth, L., Saur, J., Retherford, K.D., Feldman, P.D., Strobel, D.F.: A phenomenological model of Io's UV aurora based on HST/STIS observations. Icarus **228**, 386–406 (2014)
Roth, L., Boissier, B., Moullet, A., Sánchez-Monge, Á, de Kleer, K. et al.: An attempt to detect transient changes in Io's SO_2 and NaCl atmosphere. Icarus **350**, article id. 113925 (2020)
Roth, L., Ivchenko, N., Gladstone, G.R., Saur, J., Grodent, D., Bonfond, B., Molyneux, P.M., Retherford, K.D.: Evidence for a sublimated water atmosphere on Ganymede from Hubble Space Telescope observations. arXiv:2106.03570 (2021)
Sartoretti, P., McGrath, M.A., Paresce, F.: Disk-resolved imaging of Io with the Hubble Space Telescope. Icarus, **108**, 272–284 (1994)

Sartoretti, P., Belton, M.J.S., McGrath, M.A.: SO_2 distributions on Io. Icarus, **122**, 273–287 (1996).
Saur, J., Neubauer, F.M., Strobel, D.F., Summers, M.E.: Interpretation of Galileo's Io plasma and field observations: I0, I24, and I27 flybys and close polar passes. J. Geophys. Res. **107**(A8), 1422 (2002). https://doi.org/10.1029/2001JA005067
Saur, J., Strobel, D.F.: Relative contributions of sublimation and volcanoes to Io's atmosphere inferred from its plasma interaction during solar eclipse. Icarus **171**, 411–420 (2004)
Schneider, N.M., Bagenal, F.: Io's neutral clouds, plasma torus, and magnetospheric interaction. In: Lopes, R.M., Spencer, J.R. (eds.) Io after Galileo: A New View of Jupiter's Volcanic Moon, pp. 265–286. Springer. ISBN 3-540-34681-3 (2007)
Secosky, J.J., Potter, M.: A Hubble Space Telescope study of posteclipse brightening and albedo changes on Io. Icarus **111**, 73–78 (1994)
Sinton, W.M., Kaminsky, C.: Infrared observations of eclipses of Io, its thermophysical parameters, and the thermal radiation of the Loki volcano and environs. Icarus **75**, 207–232 (1988)
Spencer, J.R., Schneider, N.M.: Io on the eve of the Galileo mission. Annu. Rev. Earth Planet. Sci. **24**, 125–190 (1996)
Spencer, J.R., Sartoretti, P., Ballester, G.E., McEwen, A.S., Clarke, J.T., McGrath, M.A.: The Pele plume (Io): observations with the hubble space telescope. Geophys. Res. Lett. **24**, 2471–2474 (1997)
Spencer, J.R., Jessup, K.L., McGrath, M.A., Ballester, G.E., Yelle, R.: Discovery of gaseous S_2 in Io's Pele Plume. Science **288**, 1208–1210 (2000)
Spencer, J.R., Lellouch, E., Richter, M.J., López-Valverde, M.A., Lea Jessup, K., et al.: Mid-infrared detection of large longitudinal asymmetries in Io's SO_2 atmosphere. Icarus **176**, 283–304 (2005)
Spencer, J.R., Stern, S.A., Cheng, A.F., et al.: Io volcanism seen by *New Horizons*: A major eruption of the Tvashtar volcano. Science **318**, 240–243 (2007)
Strobel, D.F., Wolven, B.C.: The atmosphere of Io: abundances and sources of sulfur dioxide and atomic hydrogen. Astrophys. Space Sci. **277**, 271–287 (2001)
Strobel, D.F., Zhu, X., Summers, M.E.: On the vertical structure of Io's atmosphere. Icarus **111**, 18–30 (1994)
Summers, M.E., Strobel, D.F.: Photochemistry and vertical transport in Io's atmosphere and ionosphere. Icarus **120**, 290–316 (1996)
Trafton, L.M.: Detection of a potassium cloud near Io. Nature **258**, 690–692 (1975)
Trafton, L.M., Caldwell, J.J., Barnet, C., Cunningham, C.C.: The gaseous sulfur dioxide abundance over Io's leading and trailing hemispheres: HST spectra of Io's C^1B_2–X^1A_1 band of SO_2 near 2100 Angstrom. Astrophys.J., **456**, 384–392 (1996)
Trafton, L.M., Moore, C.H., Goldstein, D.B., Varghese, P.L., McGrath, M.A.: HST/STIS observations and simulation of Io's emission spectrum in Jupiter shadow: Probing Io's Jupiter-facing eclipse atmosphere. Icarus **220**, 1121–1140 (2012)
Tsang, C.C.C., Spencer, J.R., Lellouch, E., Lopez-Valverde, M.A., Richter, M.J., Greathouse, T.K.: Io's atmosphere: Constraints on sublimation support from density variations on seasonal timescales using NASA IRTF/TEXES observations from 2001 to 2010. Icarus **217**, 277–296 (2012)
Tsang, C.C.C., Spencer, J.R., Jessup, K.L.: Synergistic observations of Io's atmosphere in 2010 from HST-COS in the mid-ultraviolet and IRTF-TEXES in the mid-infrared. Icarus, **226**, 604–616 (2013a)
Tsang, C.C.C., Spencer, J.R., Lellouch, E., Lopez-Valverde, M.A., Richter, M.J., Greathouse, T.K., Roe, H.: Io's contracting atmosphere post 2011 perihelion: Further evidence for partial sublimation support on the anti-Jupiter hemisphere. Icarus **226**, 1177–1181 (2013b)
Tsang, C.C.C., Spencer, J.R., Jessup, K.L.: Non-detection of post-eclipse changes in Io's Jupiter-facing atmosphere: Evidence for volcanic support? Icarus **248**, 243–253 (2015)
Tsang, C.C.C., Spencer, J.R., Lellouch, E., Lopes-Valverde, M.A., Richter, J.J.: The collapse of Io's primary atmosphere in Jupiter eclipse. JGR **121**, 1400–1410 (2016)

Tsuchiya, F., Kagitani, M., Yoshioka, K., Kimura, T., Murakami, G., Yamazaki, A., et al.: Local electron heating in the Io plasma torus associated with Io from the Hisaki satellite observation. J. Geophys. Res. Space Phys. **120**, 10,317–10,333 (2015)

Wagman, D.D.: Sublimation Pressure and Enthalpy of $S0_2$. Chem. Thermodynamics Data Center, Nat. Bureau of Standards, Washington, DC (1979)

Walker, A.C., Gratiy, S.L., Goldstein, D.B., Moore, C.H., Varghese, P.L., et al.: A comprehensive numerical simulation of Io's sublimation-driven atmosphere. Icarus **207**, 409–432 (2010)

Walker, A.C., Moore, C.H., Goldstein, D.B., Varghese, P.L., Trafton, L.M.: A parametric study of Io's thermophysical surface properties and subsequent numerical atmospheric simulations based on the best fit parameters. Icarus **220**, 225–253 (2012)

Wolven, B.C., Moos, H.W., Retherford, K.D., Feldman, P.D., Strobel, D.F., Smyth, W.H., Roesler, F.L.: Emission profiles of neutral oxygen and sulfur in Io's exospheric corona. J. Geophys. Res. **106**, 26155–26182 (2001)

Wu, R.C.Y., Yang, B.W., Chen, F.Z., Judge, J., Caldwell, J., Trafton, L.M.: Measurements of high-, room-, and low-temperature photoabsorption cross sections of SO_2 in the 2080- to 2950-A region, with applications to Io. Icarus **145**, 289–296 (2000)

Yoneda, M., Kagitani, M., Tsuchiya, F., Sakanoi, T., Okano, S.: Brightening event seen in observations of Jupiter's extended sodium nebula. Icarus **261**, 31–33 (2015)

Yoshikawa, I., Yoshioka, K., Murakami, F., aYmazaki, A., Tsuchiya, F., et al.: Extreme ultraviolet radiation measurement for planetary atmospheres, magnetospheres from Earth-orbiting spacecraft (EXCEED). Space Sci. Rev. **184**, 237–258 (2014)

Zhang, J., Goldstein, D.B., Varghese, P.L., Gimelshein, N.E., Gimelshein, S.F., Levin, D.A.: Simulation of gas dynamics and radiation in volcanic plumes of Io. Icarus **163**, 182–187 (2003)

Zolotov, M.Y., Fegley Jr, B.: Volcanic production of sulfur monoxide (SO) on Io. Icarus Note **132**, 431–434 (1998)

Zolotov, M.Y., Fegley Jr., B.: Oxidation state of volcanic gases and the interior of Io. Icarus **141**, 40–52 (1999)

Zolotov, MY., Fegley Jr., B.: Eruption conditions of Pele Volcano on Io inferred from chemistry of its volcanic plume. GRL **27**, 2789–2792 (2000)